

CHARGED PARTICLE PRODUCTION IN PROTON-PROTON INCLUSIVE REACTIONS AT VERY HIGH ENERGIES

P. CAPILUPPI, G. GIACOMELLI*, A.M. ROSSI and G. VANNINI

Istituto di Fisica dell'Università and INFN, Sezione di Bologna, Bologna, Italy

A. BERTIN**, A. BUSSIÈRE*** and R.J. ELLIS

CERN, Geneva, Switzerland

Received 8 March 1974

Abstract: Experimental results on the production of charged particles in proton-proton inclusive reactions at intermediate angles (80–350 mrad) and in the momentum range of 1.5–10 GeV/c at the CERN ISR are reported. The data are presented as a function of the longitudinal variables x and y_{lab} , and of the transverse momentum p_t . For each type of observed particle the experimental distributions and their energy dependence are discussed.

1. Introduction

Particle production experiments were always among the first to be performed at each new high-energy accelerator. Most experiments were done with protons on nuclear targets and were considered to be mainly of practical importance in order to establish the quality of the beams available. The emphasis is now on the elementary proton-proton collision [1].

The experiments currently performed on these lines are classed in either exclusive measurements, which deal with a complete description of a specific channel, or inclusive ones, where for instance only one produced particle, c , is observed:

$$p + p \rightarrow c + \text{anything}, \quad (1.1)$$

independently of other secondaries. The study of both types of processes at very high energies is very attractive, since the dynamics of the proton-proton reactions is no longer affected by any kind of threshold effect.

The present interest in studying inclusive reactions may be traced to the theoret-

* Also at Università di Padova, Italy.

** On leave of absence from Istituto di Fisica dell'Università and INFN, Sezione di Bologna, Bologna, Italy.

*** Also at DPHN/HE, Saclay, France.

ical work of Feynman [2] and Benecke et al. [3] which stressed the possible appearance of simple and general properties of inelastic processes, independent of the reaction mechanisms. Thus the terms of "scaling" and of "limiting fragmentation" were introduced, and many experiments were performed to test their validities and the ways in which the "scaling region" was approached.

The CERN Intersecting Storage Rings (ISR) have provided the unique opportunity of investigating proton-proton collisions up to 63 GeV in the centre-of-mass system, corresponding to about 2 000 GeV/c for a proton beam colliding with a stationary proton target. This allowed the study of phenomena in a completely new energy region.

The results of an experiment on charged particle production in inclusive reactions at the CERN ISR are reported here. The processes studied were

$$\begin{aligned} p + p &\rightarrow \pi^\pm + \text{anything}, \\ p + p &\rightarrow K^\pm + \text{anything}, \\ p + p &\rightarrow p^\pm + \text{anything}. \end{aligned} \quad (1.2)$$

The main purposes of the investigation concern: (i) the test of the scaling hypothesis and the approach to scaling as a function of energy; (ii) the dependence on the transverse momentum; (iii) the dependence on longitudinal variables; and (iv) the study of the kaon and antiproton production with respect to pions. The measurements were carried out using a simple apparatus, consisting of a single-arm magnetic spectrometer, where particles produced at medium angles were analysed in momentum by magnets and in velocity by Čerenkov counters and time of flight. The spectrometer enabled us to measure simultaneously the production of π^\pm , K^\pm , $p(\pi^-, K^-, \bar{p})$ in the angular region of 80 to 350 mrad and in the momentum range of 1.5 to 10 GeV/c.

The data were taken using as independent variables the values of the c.m. longitudinal and transverse momenta p_\parallel and p_\perp , corresponding to a matrix in the (p_\parallel, p_\perp) plane. They will be presented in this work in terms of the Feynman x variable

$$x = 2 \frac{p_\parallel}{\sqrt{s}} \simeq \frac{p_\parallel}{p_{\parallel, \max}}, \quad (1.3)$$

where \sqrt{s} is the total c.m. energy and $p_{\parallel, \max}$ is the maximum kinematically allowed value of p_\parallel . Another useful variable is the c.m. rapidity y defined as

$$y = \frac{1}{2} \ln \left[\frac{E + p_\parallel}{E - p_\parallel} \right], \quad (1.4)$$

where E is the c.m. energy of the observed particle. To compare the data at different energies, moreover, the variable y_{lab} will be used

$$y_{\text{lab}} = y_{\text{beam}} - y, \quad (1.5)$$

where y_{beam} is the rapidity of the incoming proton beam.

The measured cross section will be given in the Lorentz-invariant form

$$f = E \frac{d^3\sigma}{d^3p}. \quad (1.6)$$

For our purposes the scaling hypothesis in the (y_{lab}, p_t) variables will be written as

$$f = f(s, y_{\text{lab}}, p_t) \xrightarrow{s \rightarrow \infty} f(y_{\text{lab}}, p_t). \quad (1.7)$$

It should be pointed out that working at medium angles enabled us to explore both the central region of the proton-proton interaction ($y_{\text{lab}} \gtrsim 2$) and the fragmentation region (y_{lab} small).

Preliminary results of the experiment were already published [4–7]. In this work the technical details of the experiment and the final results are reported. Particular attention is devoted to the analysis of the invariant cross sections in terms of the Feynman x variable and in terms of the rapidity variable. The dependence on the transverse momentum has been the subject of a separate paper [8].

Sect. 2 gives a description of the apparatus used. The experimental procedure is discussed in sect. 3. Sect. 4 explains the method of analysis of the data. The results are then presented in sect. 5, and discussed in sect. 6.

2. Apparatus

2.1. The Intersecting Storage Rings (ISR)

We shall recall briefly some features of the ISR which are particularly relevant. The CERN ISR [9] consists of two concentric and slightly distorted rings, each 300 metres in diameter. The two rings intersect horizontally eight times with a crossing angle $\alpha = 14.8^\circ$. They are filled by pulses of about 10^{12} protons ejected from the CERN Proton Synchrotron. These pulses are “stacked” horizontally in the rings to form circulating beams about 5 cm wide and 0.5 cm high, with currents up to 15 A. Owing to the small intersection angle, the interaction region has a “diamond” shape approximately 50 cm long, 5 cm wide, and 0.5 cm high. The momentum spread of each beam is about $\pm 1\%$. One of the main parameters of the ISR is the luminosity, which is defined as [10]:

$$L = \frac{N_{\text{int}}}{\sigma_{\text{int}}} = \frac{I_1 I_2}{e^2 c h_{\text{eff}} \tan \frac{1}{2} \alpha}, \quad (2.1)$$

where N_{int} is the rate of interactions occurring when the two beams collide with the interaction cross section σ_{int} , I_1 and I_2 are the currents of the two beams, c is the velocity of light, e is the electron charge, and h_{eff} is the effective height of the two intersecting beams. At the ISR, luminosities up to $4 \times 10^{30} \text{ cm}^{-2} \text{ sec}^{-1}$ have been

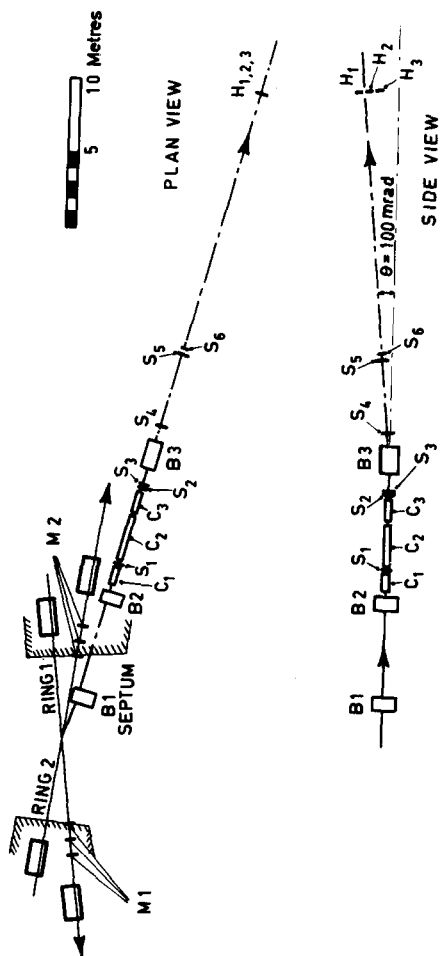


Fig. 2.1. Layout of the spectrometer: B₁-B₂ are bending magnets; S₁-S₆, H₁-H₃, and M₁-M₂ are scintillation counters; C₁-C₃ are gas threshold Cerenkov counters.

reached, with decay rates between 0.1% and 1% per hour; it was then possible to keep the beams for up to 40 hours without restacking. Such conditions were achieved mainly because of the excellent vacuum kept in the beam pipes (about 10^{-10} Torr on the average). In our intersection region, the vacuum was around 10^{-11} Torr; the background due to beam-gas interactions was then less than 10% of the total event rate.

2.2. Layout

The apparatus used for the present work (fig. 2.1) is very similar to that used in a previous experiment [11]; it contains a 46 m long single-arm spectrometer and two monitor telescopes, which all viewed intersection 2 of the ISR.

The first two magnets B_1 and B_2 allowed the production angle θ' to be changed from 80 to 200 mrad without moving the spectrometer (in the following the primed variables will refer to the ISR frame of reference). In some cases θ' was increased up to 350 mrad by moving the septum magnet B_1 30 cm away from the Beam 2 vacuum pipe. The bending magnet B_3 deflected the particles vertically upward for momentum analysis (100 mrad for H_1). The momentum bite, $(\Delta p/p)_{\text{long}} = \pm 4.5\%$, was then defined by the 20 cm height of each of the three elements H_1 , H_2 , and H_3 of the hodoscope. This hodoscope proved to be useful both for improving the statistics and for obtaining a finer grid for the measurements as a function of the rapidity variable. The particles accepted by the spectrometer had a laboratory momentum of $1.5 \text{ GeV}/c \leq p' \leq 10 \text{ GeV}/c$. This corresponds to a centre-of-mass longitudinal momentum $1.5 \text{ GeV}/c \leq p_L \leq 10 \text{ GeV}/c$, and a centre-of-mass transverse momentum $0.15 \text{ GeV}/c \leq p_t \leq 1.5 \text{ GeV}/c$ (see fig. 2.2).

The particles were detected by two telescopes of scintillation counters $S_1 S_2 S_3$ and $S_4 S_5 H_1$. S_3 was the counter which defined the solid angle ($\Delta\Omega = 2.21 \times 10^{-5}$ sr). The other counters were overmatched. The counter S_6 was used to define a "short" spectrometer, 27 m long, which was important for kaons in order to decrease the decay corrections; the momentum bite accepted by S_6 was $(\Delta p/p)_{\text{short}} = \pm 11\%$. The main parameters of the spectrometer are listed in table 2.1.

Three gas threshold Čerenkov counters C_1 , C_2 , and C_3 identified the particles as e^\pm , π^\pm , K^\pm , or p^\pm . Time-of-flight measurements were made between S_1 and H_1 and between S_1 and S_6 , to check particle identification and to discriminate between protons and heavier charged particles.

The two monitor scintillation telescopes M_1 and M_2 , common to other experiments in the intersection 2, measured the luminosity and monitored the beam conditions.

A list of the sizes and positions of the magnets and detectors used in this experiment is given in table 2.2. The amounts of materials along the spectrometer are listed in table 2.3.

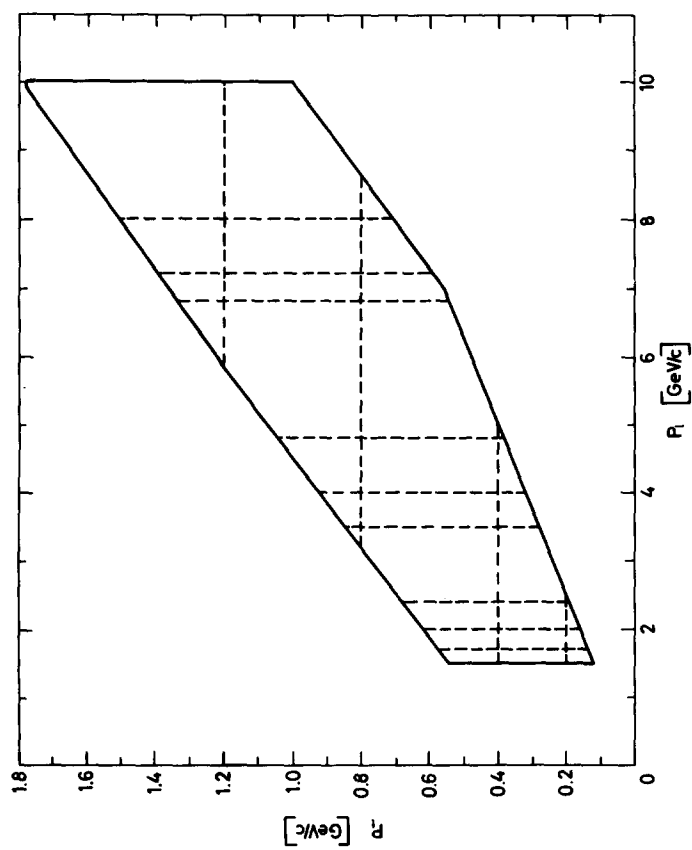


Fig. 2.2. Range in p_0 and p_t covered by the spectrometer. Some of the data have been taken along the dashed lines shown.

Table 2.1
Spectrometer parameters and allowed ranges of variables

Angular range in the ISR frame	$80 \leq \theta' \leq 350$ mrad
Particle momentum in the ISR frame	$1.5 \leq p' \leq 10$ GeV/c
c.m. longitudinal momentum	$1.5 \leq p_{\parallel} \leq 10$ GeV/c
c.m. transverse momentum	$0.15 \leq p_{\perp} \leq 1.5$ GeV/c
c.m. longitudinal x variable	$0.05 \leq x \leq 0.85$
c.m. rapidity variable	$1.0 \leq y \leq 3.2$
Momentum resolution	$(\Delta p/p)_{\text{L}} = \pm 4.5\%$ $(\Delta p/p)_{\text{S}} = \pm 11\%$
Solid angle	$\Delta\Omega = 2.21 \times 10^{-5}$ sr

Table 2.2
Sizes and locations of counters and magnets

Plastic scintillators	Dimensions (hor. \times vert. \times th.) (cm)	Distance from centre of diamond (cm)
S ₁	14 \times 8 \times 1.0	1245
S ₂	9 \times 10 \times 1.25	1790
S ₃	8 \times 9 \times 1.25	1800
S ₄	30 \times 18 \times 1.25	2200
S ₅	27 \times 30 \times 1.5	2700
S ₆	27 \times 15 \times 1.0	2725
H ₁	55 \times 20 \times 2.5	4585
H ₂	55 \times 20 \times 2.5	4588
H ₃	55 \times 20 \times 2.5	4591
Čerenkov counters	(length \times internal diameter) (cm)	Distance from centre of diamond to mirror of Čerenkov counter (cm)
C ₁	150 \times 17.5	1210
C ₂	350 \times 17.5	1600
C ₃	140 \times 17.5	1740
Magnets	Gap size (hor. \times vert. \times th.) (cm)	Distance from centre of diamond to centre of magnet (cm)
B ₁ (septum)	52 \times 5 \times 120	300
B ₂ (C)	34 \times 14 \times 100	1000
B ₃ (H)	14 \times 46 \times 200	2000
Monitor	(hor. \times vert. \times th.) (cm)	Distance from centre of diamond (cm)
M ₁₁ , M ₂₁	40 \times 20 \times 1	5700
M ₁₂ , M ₂₂	40 \times 20 \times 1	6700
M ₁₃ , M ₂₃	40 \times 20 \times 1	7700

Table 2.3
Absorbing materials in the long spectrometer

Material	Length (cm)	Length (g/cm ²)
Air	3940	4.73
Scintillators	7.9	8.3
Aluminium	1.7	4.6
Iron	0.02	0.16
Nitrogen (C ₁)	150	0.38 ^{a)}
Ethylene (C ₂)	350	2.18 ^{a)}
Ethylene (C ₃)	140	5.60 ^{a)}

a) These values are relative to a momentum $p' = 2 \text{ GeV}/c$.

2.3. Phase-space acceptance

The spectrometer viewed the whole of the interaction region; the variation in the solid angle over this rather large “diamond” was insignificant, owing to the length of the spectrometer. As already mentioned, the horizontal and vertical acceptances were defined by counter S_3 , and the momentum bite by counter H_1 for the “long” spectrometer and S_6 for the “short” one. A computer program, using beam transport matrices, was used to compute the actual particle trajectories through the magnets. The variation of the solid angle $\Delta\Omega$ with the particle momentum accepted in the spectrometer is represented in fig. 2.3. The “short” spectrometer S_6 appears to cover approximately the complete hodoscope $H_1 + H_2 + H_3$, as shown in the figure. The horizontal acceptance of the spectrometer at the diamond is plotted in fig. 2.4. Particles emitted $\pm 8 \text{ cm}$ away from the centre of the interaction region were accepted in the spectrometer with a slight variation of the production angle ($\Delta\theta = \pm 2.5 \text{ mrad}$). In the vertical plane, the spectrometer accepted particles emitted $\pm 1 \text{ cm}$ from the centre with $\Delta\phi = \pm 2 \text{ mrad}$. The total acceptance for each element of the hodoscope was typically $\Delta\Omega\Delta p/p = 1.8 \times 10^{-6} \text{ sr}$ in the centre-of-mass system (fig. 2.3) and varied slightly with each setting of the spectrometer. The exact values have been computed for each measured point.

2.4. Magnets

The 5 cm thick septum of the magnet B_1^* (see table 2.1) allowed the gap to be very close to the ISR vacuum pipe in order to accept particles produced at small angles. Special correcting coils and shielding were necessary to reduce the fringing field

* We thank the Argonne-Bologna-Michigan Collaboration for making the septum magnet available to us.

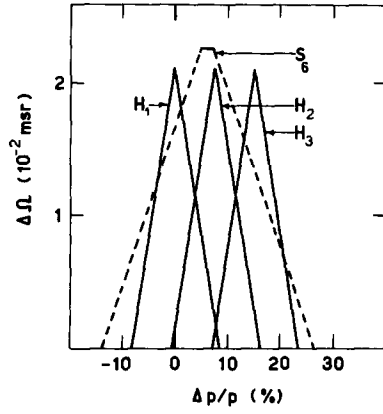


Fig. 2.3. Solid angle *versus* momentum acceptance for the short and long spectrometers at $p_{\perp} = 3 \text{ GeV}/c$ and $p_t = 0.4 \text{ GeV}/c$.

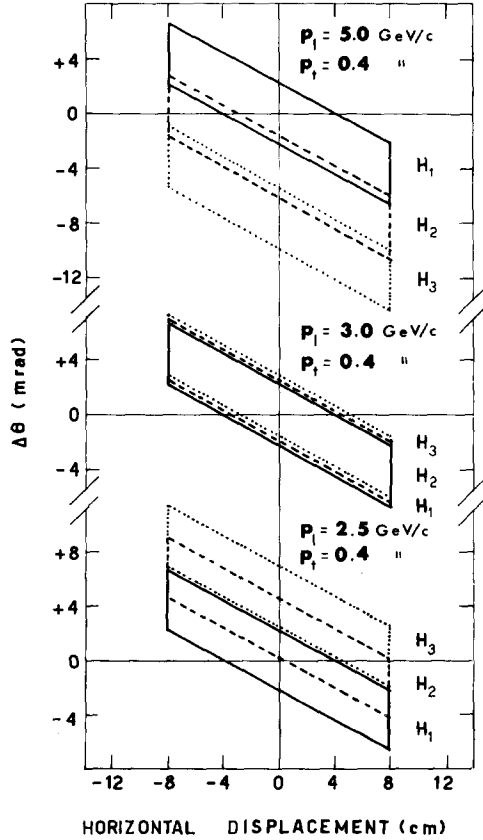


Fig. 2.4. Horizontal phase space at the diamond. The horizontal displacement is perpendicular to the average direction at emission of the accepted particles.

in order not to disturb the ISR beams. With a field integral $\int B \, dl = 15 \text{ kG} \cdot \text{metre}$, the fringing field integral was less than $5 \text{ gauss} \cdot \text{metre}$ along the ISR beam. To avoid beam losses in the ISR, all current changes were made very slowly, varying the main and the correcting coil currents together under ISR computer controls.

The other two magnets B_2 and B_3 were standard CERN PS magnets [13].

2.5. Counters

The scintillation counters were made of Pilot B plastic scintillator; the sizes and thicknesses are given in table 2.2. The light-guides, made of UVT lucite, were placed alternately to the left and to the right of the spectrometer axis to eliminate events counted by the Čerenkov radiation in the lucite. RCA 8575 and Philips 56DVP photomultiplier tubes were used. Counters S_1 and H_1 , H_2 , H_3 were viewed by two phototubes, one to the left and one to the right of each scintillator, in order to achieve a better time resolution in the time-of-flight spectra, as discussed later.

The Čerenkov counters were standard CERN threshold gas counters*; their dimensions are given in table 2.2. They had semi-spherical (aluminium) windows 3 mm thick, and were viewed by Philips 56DUVP photomultipliers. Counters C_2 and C_3 were filled with ethylene at pressures ranging from 0.5 kg cm^{-2} to 33 kg cm^{-2} (see fig. 3.1). Counter C_1 was filled either with nitrogen to measure the electron contamination when C_2 was counting pions, or with ethylene when operating in parallel with C_2 or C_3 to improve particle identification.

2.6. Electronics

2.6.1. Trigger logic. The signals from the photomultipliers were logically processed by standard CERN NIM circuitry. A schematic block-diagram of the logic is shown in fig. 2.5. The pulses from each phototube were fed into separate discriminators and the following coincidences were made: $S_{123} = (S_{1L}S_{1R}S_2S_3)$ counted all particles before B_3 ; $S_{45}H_i = (S_4S_5H_{iL}H_{iR})$ and $S_{456} = (S_4S_5S_6)$ counted particles after B_3 . The number of charged particles detected by the "long" spectrometer was then given by $L_i = (S_{123}S_{45}H_i)$, for each element of the hodoscope. For the "short" spectrometer, the corresponding number was $S = (S_{123}S_{456})$.

The effective resolving times of the L_i and S coincidences (10 nsec) were determined by the S_1 shaper. The accidental events in the spectrometer were monitored by the delayed coincidences $L_iD = (S_{123})(S_{45}H_i)_{\text{delayed}}$ and $SD = (S_{123})(S_{456})_{\text{delayed}}$. The outputs of all coincidences were recorded on 30 MHz scalars.

2.6.2. Particle identification. Three gas threshold Čerenkov counters were used to identify the particles as electrons, pions, kaons, or protons (antiprotons). In a normal

* We thank the CERN engineering Assistance Group under G. Muratori for supplying us with the threshold Čerenkov counters.

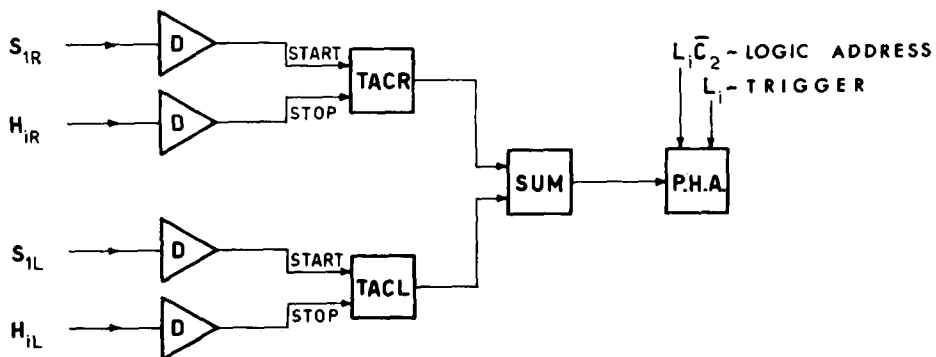
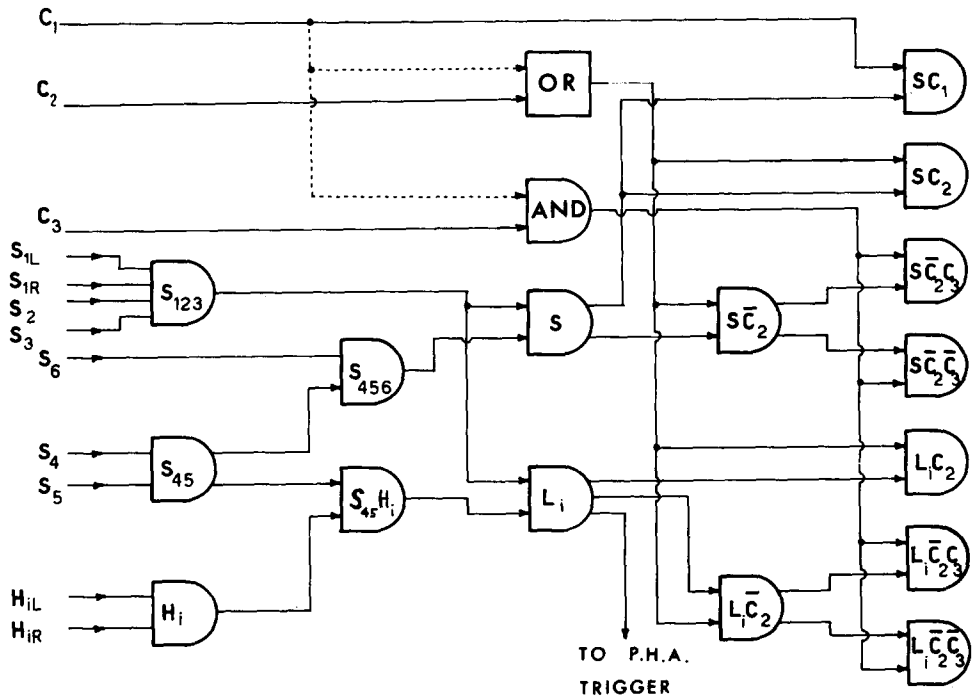


Fig. 2.5. Block diagram of the electronics, including the time-of-flight logic. The dashed lines refer to alternative logic combinations with the Čerenkovs, as explained in the text.

Table 2.4
Particle selection

Particle	Short spectrometer	Long spectrometer
e	SC_1	L_1C_1
π	SC_2 or $S(C_1 + C_2)$	L_1C_2 or $L_1(C_1 + C_2)$
K	SC_2C_3 or $SC_2C_1C_3$	$L_1C_2C_3$ or $L_1C_2C_1C_3$
p	$SC_2\bar{C}_3$	$L_1C_2\bar{C}_3$

run, C_1 was filled with nitrogen and set at a pressure below the pion threshold (dashed line in fig. 3.1), C_2 and C_3 were filled with ethylene at a pressure just above the pion and kaon knees, respectively. The maximum pressure of 33 kg cm^{-2} , above atmospheric pressure, allowed the separation of kaons from protons, only for $p' \geq 2 \text{ GeV}/c$. Below this momentum the kaons and protons (antiprotons) were identified using the time-of-flight technique. Each type of particle was selected with the proper coincidence and anticoincidence as shown in table 2.4.

Counter C_1 was also used to improve particle identification and to monitor Čerenkov efficiencies. With C_1 in parallel with C_2 , the signal $(C_1 + C_2)$ from an OR circuit was used instead of the signal C_2 (see table 2.4 and the dashed line in fig. 2.5). The efficiency of the pion identification was then improved from $(1 - \Delta\epsilon_2)$ to $(1 - \Delta\epsilon_1\Delta\epsilon_2)$, $\Delta\epsilon_1$ and $\Delta\epsilon_2$ being the inefficiencies of C_1 and C_2 , respectively. Moreover, we recorded $(SC_1\bar{C}_2)$, which gave a direct measurement of the inefficiency $\Delta\epsilon_2 = SC_1\bar{C}_2/SC_1$. With C_1 in parallel with C_3 , the coincidence signal (C_1C_3) was used instead of C_3 (see table 2.4 and the dashed line in fig. 2.5). In these conditions, a δ ray had to be produced both in C_1 and C_3 by a proton to be counted as a kaon; therefore the identification of kaons was much improved. We recorded also $(SC_1\bar{C}_3)$, which gave a direct measurement of the inefficiency $\Delta\epsilon_3 = SC_1\bar{C}_3/SC_1$ of the counter C_3 .

2.6.3. Time of flight. For each event, the times of flight (TOF) between S_1 and each hodoscope element, and between S_1 and S_6 were recorded. Fig. 2.5 shows the logic of the TOF for one hodoscope element. As already mentioned, the counters S_1 , H_1 , H_2 , and H_3 were each viewed by two photomultipliers. The TOF between the "left" and "right" pairs of phototubes ($S_{1L} - H_{1L}$) and ($S_{1R} - H_{1R}$) was measured by CERN-NIM fast discriminators and time-to-amplitude converters (TACL and TACR). The outputs of the TAC's were added, to make the TOF measurement independent of the position where the particles struck the H_i and S_1 counters, and were recorded on a 512-channel pulse-height analyser. The PHA was triggered by the L_1 coincidences. Routing pulses ($L_1\bar{C}_2$) were used to store the events in four selected subgroups of channel, one for $(\pi_1 + \pi_2 + \pi_3)$ and three for $(K + p)_i$ for each element of the hodoscope. Owing to the good time resolution (about 1 nsec), these TOF spectra allowed us to separate pions and kaons from protons, up to a momentum of 4

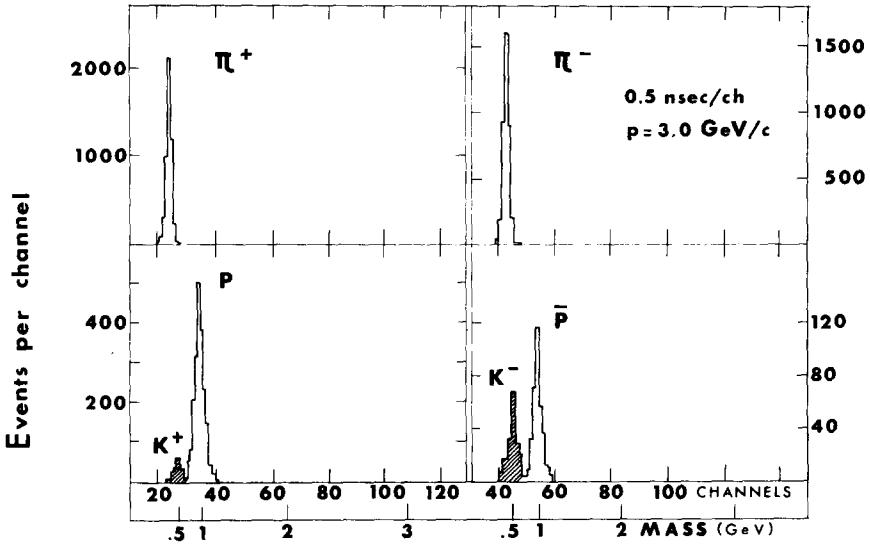


Fig. 2.6. Examples of time-of-flight spectra.

GeV/c. Fig. 2.6 shows two typical TOF spectra.

2.6.4. Gate. All coincidences and the monitors were gated with a random coincidence signal $M_{21}D$ from the M_2 monitor (see next section), for a time of $100 \mu\text{sec}$. In that way all the logic was turned off when the random coincidence rate of M_2 was too high, indicating anomalous Beam 2 background conditions arising from beam instabilities, beam-wall interactions, etc.

2.7. Monitor

Because of the lack of space around the intersection region of the ISR, the common monitoring facility [15] was not completely symmetric. Monitor M_1 consisted of a three-scintillator telescope, $M_{1B} = (M_{11B}M_{12B}M_{13B})$, just below the outgoing Beam 1 vacuum pipe (table 2.2). Monitor M_2 consisted of two three-scintillator telescopes, $M_{2A} = (M_{21A}M_{22A}M_{23A})$ and $M_{2B} = (M_{21B}M_{22B}M_{23B})$, just above and below the outgoing Beam 2 vacuum pipe, respectively (table 2.2). The following coincidences were used to monitor the beam-beam interaction: $M_1M_2 = M_{1B}(M_{2A} + M_{2B})$ and $M_{1B}M_{2B}$. Because of kinematics, the M_1M_2 coincidence counted both elastic and inelastic events, while $M_{1B}M_{2B}$ counted only the inelastic ones. Random coincidences were also counted by the delayed coincidences $(M_1M_2)_{\text{delayed}}$ and $(M_{1B}M_{2B})_{\text{delayed}}$. As discussed later, the monitor counters were used to perform the luminosity measurements.

Two other large telescopes [16], including water Čerenkov counters, scintillation

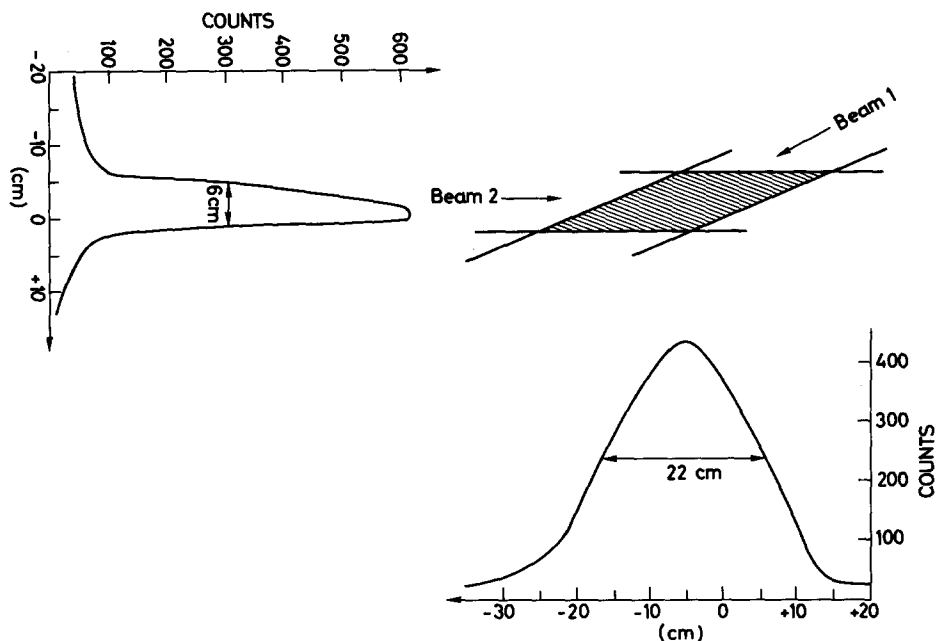


Fig. 2.7. Horizontal projections of the "diamond" as seen by a large counter telescope placed below the interaction region.

counters, and spark chambers, have been used as common facilities for all experiments in the intersection. These two installations viewed the whole interaction region, one vertically and the other horizontally, in order to monitor the size and position of the "diamond". As an example, the horizontal projection of the diamond is shown in fig. 2.7.

3. Experimental procedure

3.1. Calibrations

The septum magnet was calibrated at Argonne and at CERN, using nuclear magnetic resonances (NMR) and rotating coil techniques. The two CERN magnets were calibrated using standard tables [13] and checked by NMR probes. Absolute calibrations and stabilities were estimated to be $\pm 0.5\%$. The scintillation counters have been tested at the CERN PS to establish the high-voltage settings and to calibrate the time-of-flight system. At the end of each scintillator was placed a ^{247}Am , α source embedded in a small scintillator disc, in order to check periodically the response of the detectors. The rate of about 10^3 α /sec was large enough to perform quick calibrations and small enough to give rise to negligible accidentals. Calibrations with α

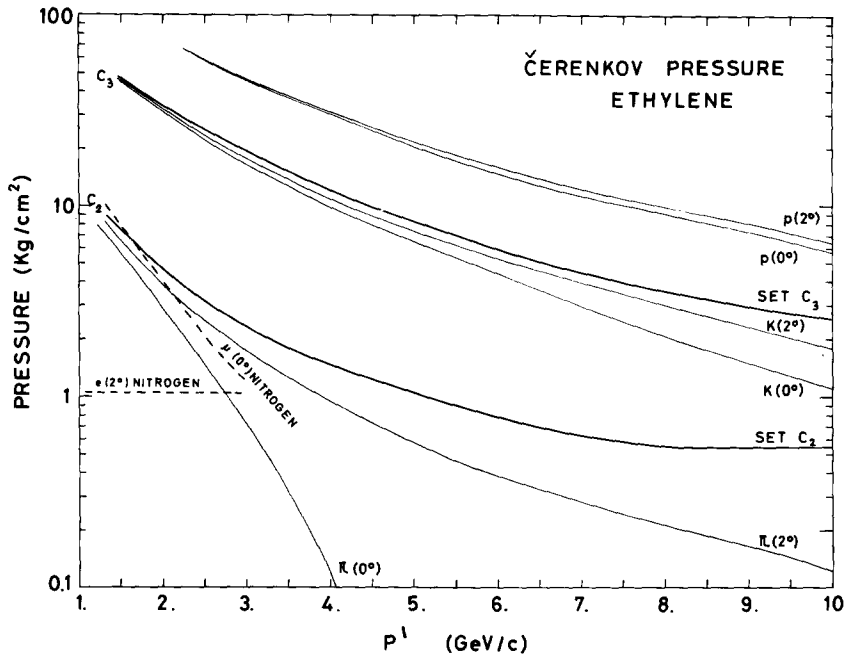


Fig. 3.1. Curves used for the actual settings of the gas threshold Čerenkov counters versus particle momentum. Also shown are the curves for the threshold values and for Čerenkov light emitted at 2° . The dashed lines correspond to the threshold values for muons and to the 2° curve for electrons in nitrogen. Pressures are above atmospheric.

sources were particularly useful at the beginning of the ISR operation, when the luminosity and hence the counting rates in our telescope were small.

The Čerenkov counters were tuned at the PS. The efficiencies were found to be greater than $0.999 = \epsilon_2 (= 1 - \Delta\epsilon_2)$ for C_2 and $0.99 = \epsilon_1 = \epsilon_3$ for C_1 and C_3 . From these measurements, the reference plots of pressure settings versus particle momentum, shown in fig. 3.1, were obtained.

All the magnets and counters were aligned along the spectrometer axis. The accuracy of the position was ± 0.5 cm longitudinal and ± 0.2 cm transverse.

Since the experiment lasted about 20 months, the following extended checking procedure was established at the beginning of each ISR period (~ 1 month):

- (a) Check of the magnet calibrations with a nuclear magnetic resonance probe.
- (b) Test of the scintillation counters with the α sources and eventually with a ^{60}Co source.
- (c) Survey of the positions of the counters and magnets.
- (d) Check of the Čerenkov pressure curves.
- (e) Check of the high-voltage curves.
- (f) Timing of the electronics.

(g) Time-of-flight check.

(h) Measurement of the Čerenkov counters' efficiencies.

Moreover, at the beginning of each ISR run, a simple checking procedure was applied including α source test, pulse-widths control, high voltage, delay checks, etc.

3.2. Luminosity determination

At the beginning of most ISR runs, a luminosity measurement was performed in all intersection regions simultaneously, using the Van der Meer method [10] of displacing the two beams vertically apart, one from the other. Practically, the two ISR beams were displaced in sets of 0.5 mm, using a complex set of steering magnets. For each setting, the monitor rate MM was recorded to obtain curves such as the ones shown in fig. 3.2. The luminosity curves were obtained at different periods, under various conditions (normal, after the "shaving" technique, with the "Terwilliger"

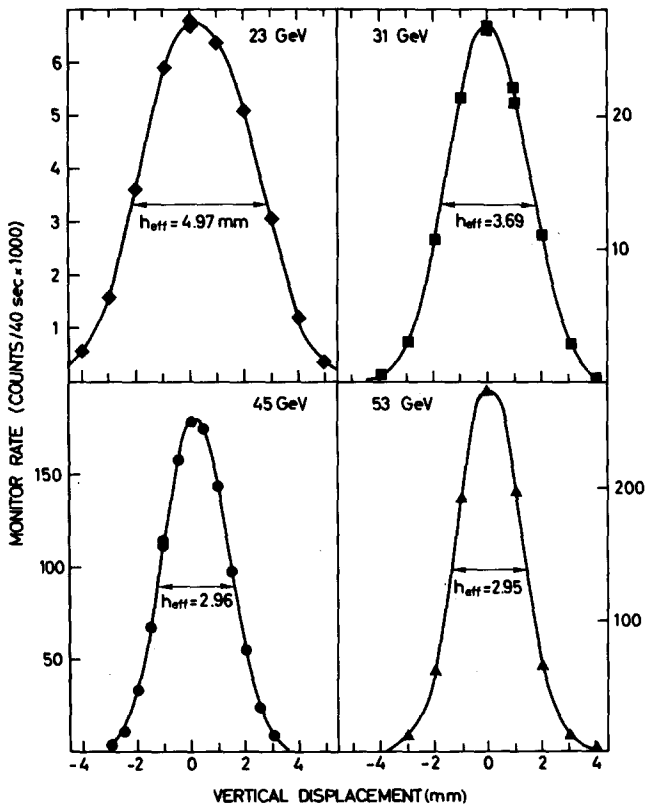


Fig. 3.2. Examples of luminosity curves at four different energies.

scheme, etc.). From such curves the effective height of the two intersecting beams can be extracted as:

$$h_{\text{eff}} = \frac{\sum MM}{MM_{\text{max}}}, \quad (3.1)$$

where MM_{max} is the maximum counting rate of the monitor at the peak and $\sum MM$ is the summation over the curve, i.e. the area under the luminosity curve; Van der Meer has shown that this h_{eff} is equal to the value obtained by folding the two beams, provided that the vertical profile of each beam does not change when the beams are moved away from the ISR median plane.

The luminosity is then calculated as (see expression (2.1)):

$$L = \frac{I_1 I_2}{e^2 c h_{\text{eff}} \lg \frac{1}{2} \alpha} \approx \frac{I_1 I_2}{\sum MM} MM_{\text{max}} \cdot 100 \text{ mb}^{-1} \text{ sec}^{-1}. \quad (3.2)$$

In fact, the losses and blowing up of the beams made the luminosity vary during a single ISR run. The luminosity was therefore continuously monitored as:

$$L = \frac{K_M MM}{e^2 c \lg \frac{1}{2} \alpha}, \quad (3.3)$$

with the monitor constant K_M defined as

$$K_M = \frac{I_1 I_2}{\sum MM}. \quad (3.4)$$

K_M is determined more accurately than h_{eff} and is directly used in the computation of the cross section:

$$\frac{d^2 \sigma}{d\Omega dp} = \frac{N e^2 c \lg \frac{1}{2} \alpha}{K_M MM \Delta\Omega \Delta p}, \quad (3.5)$$

where N is the rate of particles detected in the phase-space acceptance $\Delta\Omega \Delta p$. During our 20 months running period, several changes were made around the intersection 2, to improve the machine conditions or to install new equipment. The monitoring conditions and hence the monitor constant were in some cases affected. However, the K_M value was systematically measured two or three times per week and then averaged over that period for which the experimental conditions of the monitors were the same. Fig. 3.3 shows typical averaged values of K_M as a function of the ISR energies. Both the reproducibility and the absolute accuracy of the monitor constant were improving with time; the ISR luminosity scheme was changed (4-magnet bump

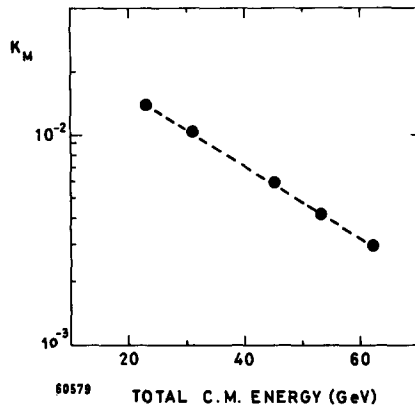


Fig. 3.3. The monitor constant K_M versus c.m. energy for a specific monitor configuration.

instead of 2-magnet bump) [17] to minimize interferences among the intersections, and the absolute scale of the displacement was checked and corrected. While at the end of 1971 it was difficult to obtain $\pm 10\%$ accuracy, the error on the monitor constant K_M was typically $\pm 3\%$ at the end of the experiment. Since this error affects the cross-section directly, it has to be emphasized that the precision in the determination of the luminosity is of the greatest importance for any absolute measurement of cross section, and in particular for any comparison between different ISR energies.

3.3. Data taking

In a standard ISR physics run of about 20 hours, the two rings were each filled with 3-5 A of protons; the beams were optimized and a luminosity measurement was performed. The beams were then usually dumped and restacked at high currents such as 5-15 A. Our runs were of about one hour duration. Pion, kaon, proton (antiproton), and monitor rates were recorded, as well as other information useful for checking and ensuring reliability of the data (for instance the following counting rates: S_{123} , S_{45} , S_{456} , $S_{456}H_i$, S , L_i , $L_i\bar{C}_2$, randoms, number of gate signals, etc.).

At the end of each one-hour run, the consistency of the data among the scalers and with the time-of-flight spectra was checked, and inefficiencies of the Čerenkov counters were computed (see subsect. 2.6). Accidental events in the spectrometer were found to be always negligible. At least once every ISR run, the following information was recorded:

- (i) the readings of four vacuum gauges located close to the intersection region;
- (ii) The size and position of the "diamond" as obtained by the horizontal and vertical common monitor of the intersection (see fig. 2.7).

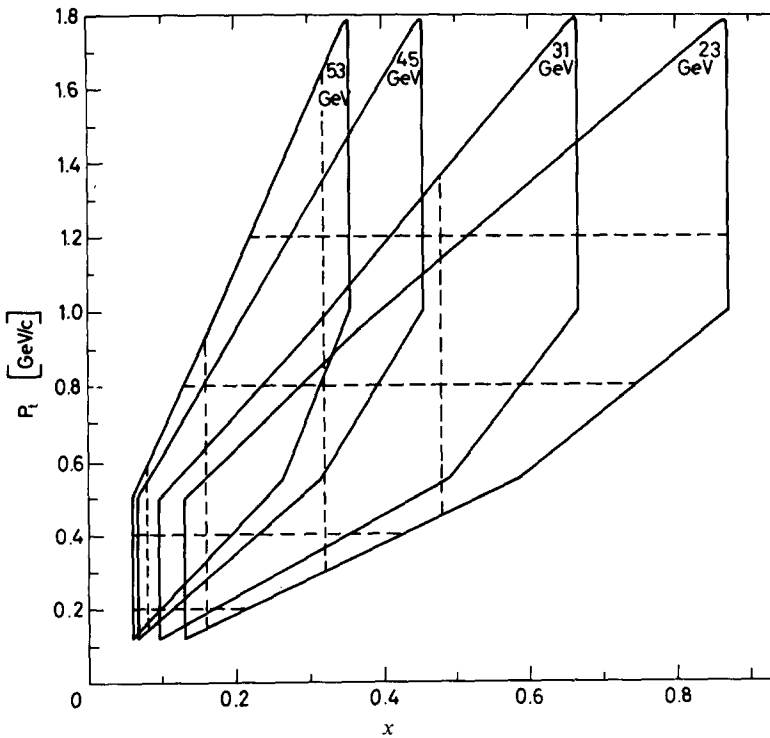


Fig. 3.4. Illustration of the acceptance of the spectrometer in x and p_t . Data were taken along the dashed lines shown, at constant values of x or of p_t .

3.4. Range of measurements

Since for a given energy the cross-section is a function of two independent variables, the production cross section has been measured

(i) as function of x and y_{lab} at $p_t = 0.2, 0.4, 0.8$, and $1.2 \text{ GeV}/c$, for all particles (π^+ , π^- , K^+ , K^- , p and \bar{p});

(ii) as function of p_t at $x = 0.08, 0.16, 0.32$, and 0.48 for all particles, except at $x = 0.48$ where only positive particles were recorded;

(iii) as function of p_t at fixed values of y_{lab} , for $0.5 < y_{\text{lab}} < 2.5$.

Figs. 3.4 and 3.5 show the measured points (dashed lines) within the acceptance of our spectrometer ($0.05 < x < 0.85$ and $1.0 < y < 3.2$).

Data were taken at the five ISR operational energies 2×11.7 , 2×15.4 , 2×22.5 , 2×26.7 , and $2 \times 31.4 \text{ GeV}$. At 11.7 GeV and 31.4 GeV , the small luminosity available limited the amount of data we could take. The total number of events recorded was about 5×10^5 , corresponding to 170 different data points.

Table 3.1 is a list of the parameters corresponding to the various ISR energies.

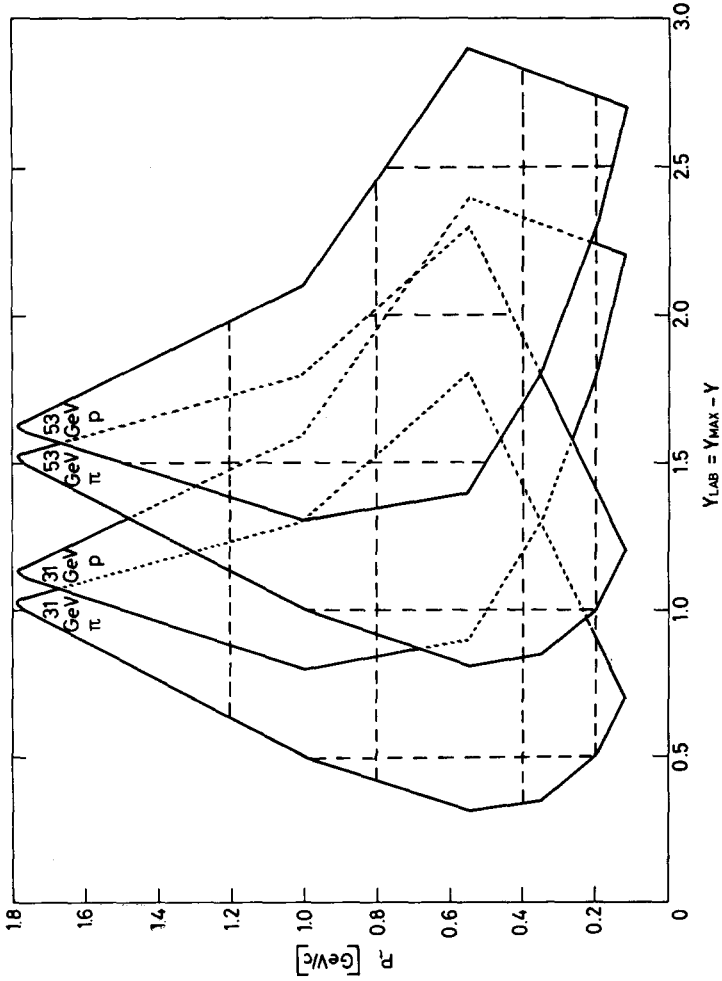


Fig. 3.5. Illustration of the acceptance of the spectrometer in Y_{LAB} and p_t . Data were taken along the dashed lines shown, at constant values of Y_{LAB} or of p_t .

Table 3.1
ISR parameters

p_{beam} (GeV/c)	11.7	15.4	22.5	26.7	31.6
E_{cm} (GeV)	23.3	30.6	44.6	53.0	62.7
s (GeV ²)	543	936	1990	2810	3930
p_{lab} (GeV/c)	289	498	1060	1500	2090
y_{beam}	3.21	3.48	3.86	4.03	4.20
L_{max} (10 ³⁰ cm ⁻² sec ⁻¹)	0.1	0.6	4.0	4.0	0.1

4. Analysis and corrections

4.1. Computation of cross sections

The experimental cross sections were determined as:

$$\frac{d^2\sigma}{d\Omega dp} = \frac{N}{K_M MM \Delta\Omega \Delta p} e^2 c \lg \frac{1}{2}\alpha, \quad (4.1)$$

where N is the rate of events (π^+ , π^- , and p : long spectrometer; K^+ , K^- and \bar{p} : short spectrometer), and MM ($= MM - MM_{\text{delayed}}$) the rate of events recorded by the monitor; K_M is the monitor constant, discussed in subsect. 3.2; $\Delta\Omega \Delta p$ is the phase space accepted by the spectrometer, see subsect 2.3. The cross sections were calculated in the c.m. frame, transformed to the Lorentz invariant form and corrected as

$$\frac{Ed^3\sigma}{d^3p} = \frac{E}{p^2} \frac{d^2\sigma}{d\Omega dp} F_D F_M F_A F_E F_K F_B, \quad (4.2)$$

where E and p are the total energy and momentum of the produced particles; the F 's are the various correction factors discussed in the next two subsections.

4.2. Corrections

The raw cross sections have been corrected for the following effects:

- (i) decay of unstable particles (F_D);
- (ii) multiple Coulomb scattering (F_M);
- (iii) absorption of the particles in materials along the spectrometer (F_A);
- (iv) electron (positron) contamination in the recorded pion rates (F_E);
- (v) Čerenkov counter efficiencies and δ rays produced by protons (F_K);
- (vi) beam-gas collisions (F_B).

Other corrections, such as corrections to the pion rates arising from $K_S^0 \rightarrow \pi^+ \pi^-$ decay, have not been applied, since each pion was measured in an inclusive reaction, independently of its origin.

The decay and multiple Coulomb scattering corrections were computed with a

Monte Carlo program, while all the other corrections were calculated on the basis of measurements. The Monte Carlo program generated particles, with initial parameters determined from uniform random distributions in a spatial region representing the actual interaction region (source). The particles were then traced through the spectrometer, a first time without any effect (such as decay or scattering) in order to determine the final number of particles accepted by the "geometry"; a second time with the effects considered giving the "corrected" number of particles. The correction factor was derived as the ratio of these two numbers:

$$F = N_{\text{geometry}} / N_{\text{corrected}} \quad (4.3)$$

4.2.1. Decay. Decay corrections were applied to pion and kaon data. The charged decay products of a pion or a kaon emitted in the forward direction has a probability of being counted as pions or kaons. In the computation of this effect, only the following two-body decays, with their branching ratios, were considered: $\pi \rightarrow \mu\nu$, $K \rightarrow \mu\nu$, and $K \rightarrow \pi\pi$. Decay products from other decay channels were assumed to be lost. Fig. 4.1 shows the pion and kaon decay correction factor F_D for the long and short spectrometers. The values computed by the Monte Carlo program are presented in table 4.1. In the momentum interval from 1.5 to 10 GeV/c, F_D for pions range from 1.35 to 1.04, for the long spectrometer, with an error of 5% to 1%, respectively. As one can see in fig. 4.1, the kaon decay correction factor for the long spectrometer be-

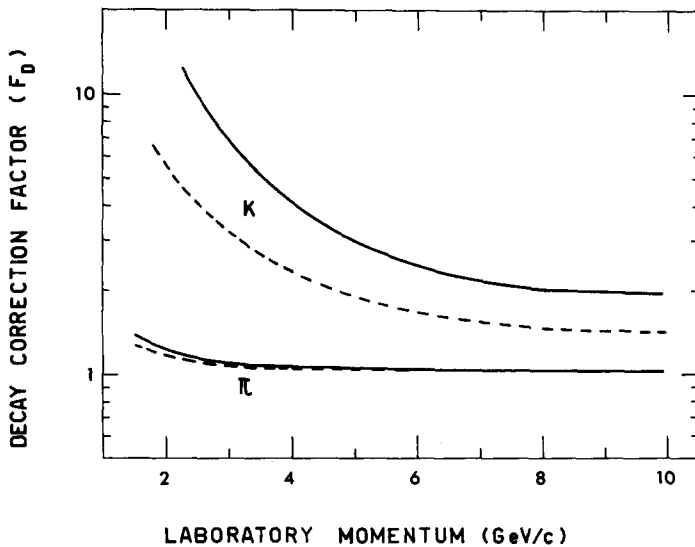


Fig. 4.1. The decay correction factor F_D versus the particle momentum p' . The solid (dashed) lines refer to the long (short) spectrometer.

Table 4.1
Decay correction factor for pions and kaons (long and short spectrometer, respectively)

p' (GeV/c)	$F_D(\pi)$	$F_D(K)$
1.5	1.35	
2.0	1.22	5.9
2.5	1.15	4.0
3.0	1.11	3.1
4.0	1.08	2.2
5.0	1.06	1.9
6.0	1.04	1.7
8.0	1.04	1.6
10.0	1.04	1.5

comes too large at low momentum. This is the reason why the short spectrometer was used for kaons. The correction factors F_D for kaons, given in table 4.1, range from 5.9 to 1.5 in the momentum interval from 2 to 10 GeV/c with an error ranging from 10% to 3%, respectively. No data on kaons below 2 GeV/c are given because of the too large decay correction.

4.2.2. Multiple Coulomb scattering. Loss of particles owing to multiple Coulomb scattering was computed by the Monte Carlo program, using the Moliere theory. Horizontal and vertical out-scatterings as well as horizontal and vertical in-scatterings were computed, with the following results:

(i) The wall of the vacuum chamber did not contribute sensitively to the loss of particles, because out-scattering was compensated by in-scattering. Therefore the multiple scattering correction was found to be almost independent of the emission angle of the particle.

(ii) In the vertical direction, in-scattering was found to be nearly equal to out-scattering. This was due to the vertical momentum analysis performed by the magnet B_3 . Then multiple scattering was significant only in the horizontal direction. Moreover, it was almost negligible for the short spectrometer.

Fig. 4.2 shows the multiple scattering correction factor F_M for pions *versus* p' , for the long spectrometer. The points correspond to the values computed by the Monte Carlo program. Interpolated values are presented in table 4.2; F_M is equal to 1.18 at 1.5 GeV/c, decreases rapidly with increasing momentum, and is almost negligible above 2.5 GeV/c. The errors on F_M are about 2%. The corresponding results are given in table 4.2 for protons.

4.2.3. Absorption. The amount of material along the spectrometer caused a reduction of the number of particles detected, owing to elastic and inelastic scattering. On the other hand some in-scattering effect was present, mainly in the last part of the

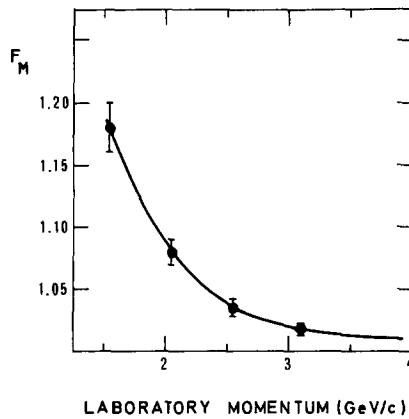


Fig. 4.2 The correction factor for multiple Coulomb scattering F_M versus p' .

Table 4.2

Multiple Coulomb scattering correction factor for pions and protons. This correction factor is negligible for the short spectrometer

p' (GeV/c)	$F_M(\pi)$	$F_M(p)$
1.5	1.18	1.22
2.0	1.08	1.10
2.5	1.04	1.05
3.0	1.02	1.02
4.0	1.01	1.01
6.0	1.01	1.01
8.0	1.01	1.01
10.0	1.01	1.01

spectrometer, due to diffraction scattering and to particles produced in the forward direction.

For each particle $c(\pi, K, p)$ the total cross section $\sigma_{\text{tot}}(c, A)$ on the complex nucleus A was computed with an interpolating formula, starting from the experimental data available in the literature [18] for the total cross sections on carbon and copper. For each particle the collision lengths L_{coll} for all the materials along the spectrometer were then derived as a function of particle momentum. The errors on L_{coll} were about 10-15% for K^\pm and \bar{p} , and about 15-20% for π^\pm and p . The absorption correction factor was defined as

$$F_A = e^{-\sum_i \epsilon_i l_i / L_{\text{coll}}}, \quad (4.4)$$

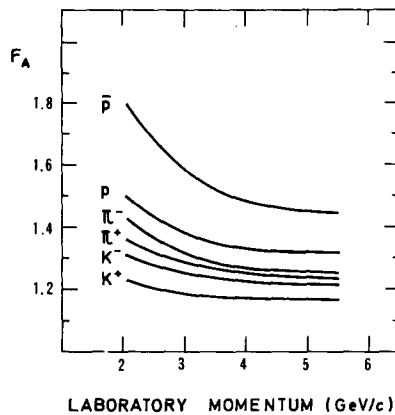


Fig. 4.3. The absorption correction factor F_A versus p' .

Table 4.3

Absorption correction factor for pions and protons (long spectrometer), kaons and antiprotons (short spectrometer)

p' (GeV/c)	$F_A(\pi^+)$	$F_A(\pi^-)$	$F_A(K^+)$	$F_A(K^-)$	$F_A(p)$	$F_A(\bar{p})$
1.5	1.36	1.39			1.50	1.73
2.0	1.38	1.42	1.22	1.30	1.56	1.81
2.5	1.33	1.36	1.20	1.27	1.46	1.66
3.0	1.29	1.31	1.18	1.24	1.38	1.55
4.0	1.26	1.27	1.17	1.23	1.36	1.45
6.0	1.22	1.23	1.15	1.21	1.32	1.38
8.0	1.21	1.22	1.14	1.19	1.31	1.36
10.0	1.21	1.22	1.13	1.18	1.30	1.35

where Σ_i is the summation over all the materials, each of length l_i (given in table 2.3) in the spectrometer, and ϵ_i is the corresponding rejection efficiency. The rejection efficiency was determined experimentally by inserting absorbers of different materials in several positions along the spectrometer. It was found to be 0.90 ± 0.12 between the B_2 and B_3 magnets and 0.6 ± 0.2 after B_3 , independent of momentum within error. For the vacuum chamber wall, where in-scattering effect due to nuclear interactions was not negligible, a rejection efficiency of $\epsilon = 0.70$ was used. Because of the very thin wall of the vacuum chamber (0.2 mm), the corresponding absorption correction was found to be less than 5%, whatever the type of particle and its emission angle.

Fig. 4.3 shows the behaviour of the absorption correction factor F_A in the momentum interval $2.0 \leq p' \leq 5.5$ GeV/c. Table 4.3 presents values of F_A for the various particles. The errors on F_A range from 6% to 1%.

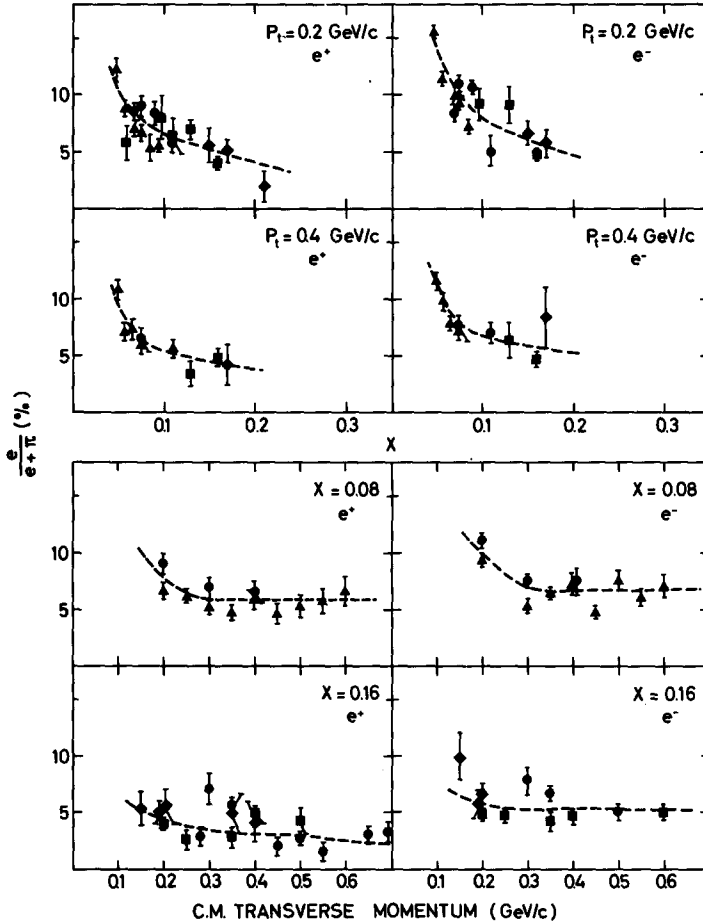


Fig. 4.4. The electron and positron contamination. The measured contaminations are shown versus x for fixed values of p_t , and versus p_t for fixed values of x .

4.2.4. Electron (positron) contamination. Neutral particles such as π^0 , K^0 , etc., produced in proton-proton interactions, decay into γ rays, which may convert into positron-electron pairs in the material around the interaction region. To identify the electrons (positrons) accepted by the spectrometer, the C_1 Čerenkov counter was filled with nitrogen and set at a pressure below the pion threshold (dashed line in fig. 3.1), and the number of electrons (positrons) was measured by SC_1 (see subject. 2.6). However, above 3 GeV/c the plateau in the pressure curve becomes too narrow to ensure a good discrimination between π and e : the electron contamination was then measured only below 3 GeV/c. Fig. 4.4 shows the measured ratios, $SC_1/SC_2 =$

Table 4.4

Correction factor for pions due to electron (positron) contamination

		p_t (GeV/c)						
x		0.2	0.3	0.4	0.5	0.6	0.8	1.20
$F_E(\pi^+)$	0.05	0.89	0.89	0.90	0.91	0.92	0.92	0.92
	0.10	0.93	0.94	0.95	0.95	0.95	0.95	0.95
	0.20	0.96	0.96	0.96	0.97	0.97	0.97	0.97
	0.30	0.97	0.97	0.97	0.97	0.97	0.97	0.97
	0.50	0.97	0.97	0.97	0.97	0.97	0.97	0.97
		p_t (GeV/c)						
x		0.2	0.3	0.4	0.5	0.6	0.8	1.20
$F_E(\pi^-)$	0.05	0.86	0.87	0.88	0.88	0.88	0.88	0.88
	0.10	0.92	0.93	0.93	0.93	0.93	0.93	0.93
	0.20	0.95	0.95	0.95	0.95	0.95	0.95	0.95
	0.30	0.95	0.95	0.95	0.95	0.95	0.95	0.95
	0.50	0.95	0.95	0.95	0.95	0.95	0.95	0.95

$e/(e + \pi)$, as a function of x (for p_t fixed) and of p_t (for x fixed); the dashed lines represent the interpolations used to correct the pion data. The electron correction factor was defined as

$$F_E = \frac{\pi}{e + \pi} = 1 - \frac{e}{e + \pi}. \quad (4.5)$$

Table 4.4 presents the values used for F_E . The errors are always less than 1%.

4.2.5. Čerenkov efficiencies and δ rays. As explained in subsect. 2.6, the inefficiencies of the Čerenkov counters C_1 , C_2 , and C_3 were continuously tested during the data-taking and found to be very stable. The average values were $\epsilon_1 = 1 - 3.5 \times 10^{-3}$, $\epsilon_2 = 1 - 4.6 \times 10^{-4}$, and $\epsilon_3 = 1 - 6.8 \times 10^{-3}$. Since these efficiencies were relatively high, no corresponding correction was applied to the data.

When a proton passed through the spectrometer it could produce a δ ray in the gas of the Čerenkov counter. If this happened in C_3 , the proton was counted as a kaon. To measure this effect, the number of protons counted by the $L_1\bar{C}_2\bar{C}_3$ coincidences was compared with the corresponding number recorded by the time-of-flight spectra. The percentage of the protons missed by the scaler is shown in fig. 4.5, as a function of the gas pressure in C_3 . The effect turned out to be negligible for the protons, but could become important for the positive kaons since the ratio p/K^+ is large. The δ rays correction factor F_K was applied to the kaon data:

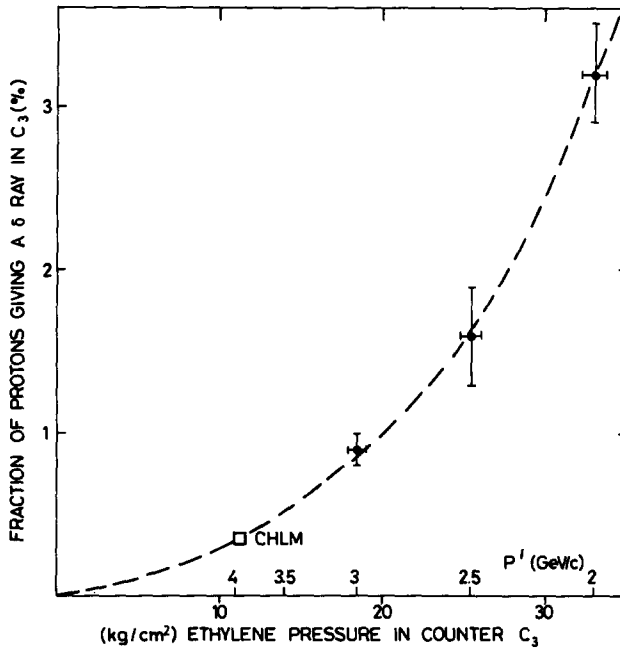


Fig. 4.5. Fraction of protons giving a δ ray in the Čerenkov counter C_3 as a function of the gas pressure.

$$F_K = 1 - \left(\frac{p_{\text{TOF}} - p_{\text{scaler}}}{p_{\text{scaler}}} \right) \frac{p}{K^+}. \quad (4.6)$$

The factor F_K ranged from 0.80 to 1.0 with a maximum error of 5%. In the momentum range explored, since the numbers of K^- and \bar{p} were of the same order of magnitude, the correction was negligible for the K^- and \bar{p} data, which therefore were not corrected for this effect.

4.3. Background

4.3.1. Beam-gas. The data have been also corrected for beam-gas background. This background arose from the interaction of the beams with the residual gas in the intersection region. Since during this experiment the pressure in the intersection region was around 10^{-11} Torr, the beam-gas background was less than 10% of the beam-beam interactions. The beam-gas background was measured by running with only Beam 1 or Beam 2. Owing to the high directionality of the spectrometer, no event coming from interactions between Beam 1 and the residual gas was recorded. Therefore the beam-gas background was measured with Beam 2 only. The beam-gas back-

ground correction factor was then

$$F_B = \frac{BB}{BB + BG} = 1 - \frac{BG}{BB + BG} = \frac{1}{1 + BG/BB}, \quad (4.7)$$

where $(BB + BG)$ was the number of events recorded in normal beam-beam runs (beam-beam + beam-gas) and BG the number of events recorded in the runs with Beam 2 only.

The beam-beam and beam-gas rates are defined as

$$BB = \frac{I_1 I_2}{e^2 c h_{\text{eff}} \tan \frac{1}{2} \alpha} \frac{d^2 \sigma_{BB}}{d\Omega dp} \Delta\Omega \Delta p, \quad (4.8)$$

$$BG = \frac{I_2}{e} \rho \frac{d}{\sin \theta} \frac{d^2 \sigma_{BG}}{d\Omega dp} \Delta\Omega \Delta p, \quad (4.9)$$

where ρ is the density of gas (particles per cm^3) and $d/\sin \theta = l$ is the length of the vacuum pipe of Beam 2 viewed by the spectrometer, which is inversely proportional to the sine of the spectrometer angle θ . Then

$$\frac{BG}{BB} = c e \tan\left(\frac{\alpha}{2}\right) \rho d \frac{h_{\text{eff}}}{I_1 \sin \theta} \left[\frac{d^2 \sigma_{BG}/d\Omega dp}{d^2 \sigma_{BB}/d\Omega dp} \right]. \quad (4.10)$$

Assuming that scaling holds, the ratio of the cross sections can be considered approximately constant; therefore, if ρ is constant,

$$\frac{BG}{BB} \frac{I_1 \sin \theta}{h_{\text{eff}}} = F_0 \approx \text{const.} \quad (4.11)$$

Fig. 4.6 shows the values of F_0 for the background runs: F_0 can be considered constant within errors. An average value of F_0 was extracted for each type of particle and the measured data were corrected by

$$F_B = \frac{1}{1 + F_0 h_{\text{eff}}/I_1 \sin \theta}. \quad (4.12)$$

Because of the increase in beam intensity and the decrease of h_{eff} , the ratio BG/BB went down by a factor of about 4 during this experiment. The correction factor F_B ranged between 0.80 and 0.99 with a typical value of 0.95. The uncertainty, mainly due to the error on F_0 , was about 3%.

4.3.2. Beam-wall. For our spectrometer, this kind of background could arise only from the interaction of Beam 2 with the vacuum pipe near the intersection. Owing to the good control on the position and size of the beams, beam-wall interaction occurred only occasionally, giving splashes of events. To avoid this type of background,

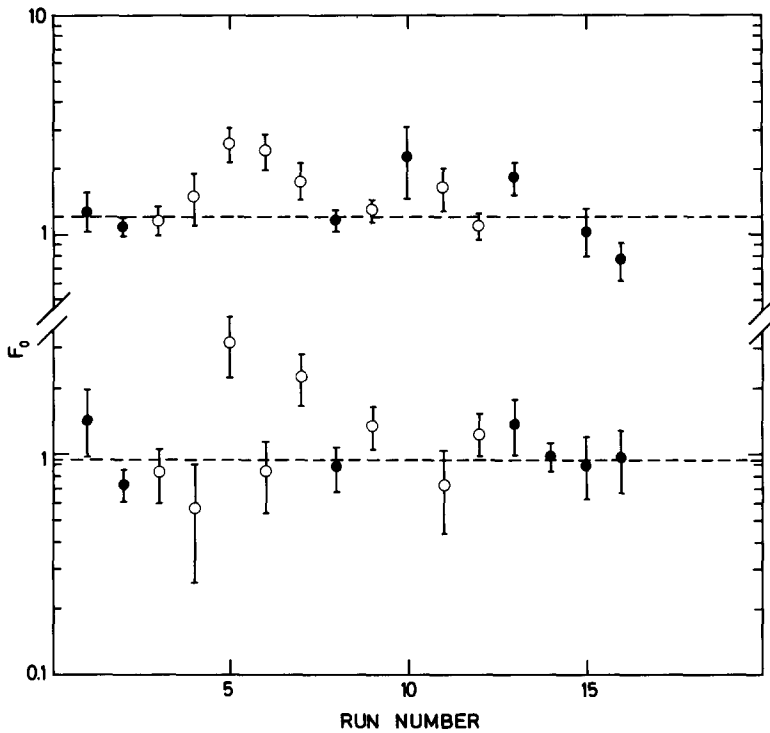


Fig. 4.6. The beam-gas background constant F_0 for positive (black points) and negative (open points) pions for the short and long spectrometer.

a gate, which turned off the electronics, was used as discussed in subsect. 2.6. The gate was closed by any anomalous increase of the number of particles coming from Beam 2, i.e. when some Beam-2 protons were striking the wall of the vacuum chamber.

Any possible contribution of a slight continuous creeping of Beam 2 along the walls would also be present in the runs with Beam 2 only; such contributions would be included in the F_B factor.

4.4. Errors

The over-all error on each data point was obtained by adding quadratically the statistical error, the error on the correction factors and on the determination of the monitor constant K_M . The statistical error ranged from 3% to 10% (typically 5%) for π^+ , π^- , and p , from 8% to 30% (typically 15%) for K^+ , K^- , and \bar{p} .

The total error on the correction factors was always between 5% and 10%, including the error on the background correction. The uncertainty on the measured value of the monitor constant K_M decreased during the period of data taking from 10% to 3%.

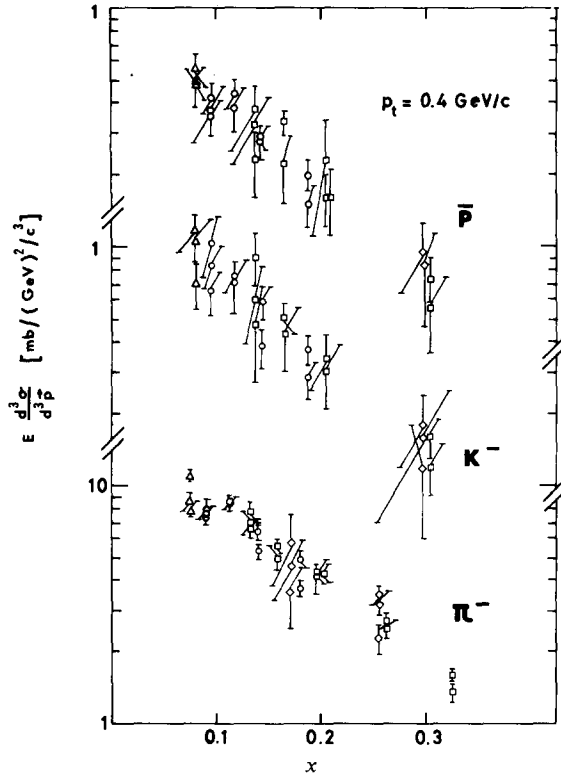


Fig. 4.7. Illustration of the reproducibility of the measurements. Data points with the same values of x were obtained in different runs under different conditions.

A test of the internal consistency of the methods used both in the analysis and in the data taking is given by the reproducibility of the results: most of the data points were measured several times under different conditions (beam currents, h_{eff} , background, monitoring, etc.). The reproducibility of the data was found to be good, within errors. Fig. 4.7 is an example of the reproducibility of our data at $p_t = 0.4 \text{ GeV}/c$ for negative particles.

A systematic scale error of few per cent, arising from the method used for the luminosity determination, cannot be excluded.

5. Results

The final cross sections are presented in the Lorentz-invariant form

$$f = E \frac{d^3\sigma}{d^3p}, \quad (5.1)$$

for all charged particles. Data have been analysed as a function of a longitudinal variable (x or y_{lab}) for fixed values of the transverse momentum p_t , and as a function of the transverse momentum for fixed values of x or y_{lab} .

5.1. Cross sections versus x and y_{lab}

The data taken at the values of $p_t = 0.2, 0.4, 0.8$, and 1.2 GeV/ c are presented in table 5.1. For π^+ , π^- , and p , the “long” spectrometer was used, giving rise to slightly different values of the transverse momentum p_t for the three elements of the hodoscope. The K^+ , K^- , and \bar{p} were recorded by the “short” spectrometer, with a transverse momentum close to the value corresponding to the first element H_1 of the hodoscope (fig. 2.3). In the following figures, the cross sections have been corrected for these differences in p_t , using the simple exponential form

$$f^{\text{figure}} = f^{\text{table}} e^{-B\Delta p_t}, \quad (5.2)$$

with the proper values for the slope B [8]. This procedure introduced negligible errors ($\leq 1\%$) since Δp_t was always less than 10% of the value of p_t .

Figs. 5.1 to 5.5 show the invariant cross sections for the inclusive production of pions, kaons, and protons (antiprotons) respectively, as a function of the Feynman variable x , at fixed values of the transverse momentum $p_t = 0.2, 0.4, 0.8$, and 1.2 GeV/ c . The same cross sections are also presented in figs. 5.6 to 5.11, but as a function of the longitudinal rapidity y_{lab} . For comparison the figures show dashed lines obtained by interpolation through published data at $\sqrt{s} = 6.8$ GeV [19, 20].

The ratios of the invariant cross sections for particle to antiparticle, π^+/π^- , K^+/K^- , and p/\bar{p} , are presented in figs. 5.12 and 5.13, as a function of y_{lab} , at fixed values of the transverse momentum. The ratios of the invariant cross sections for particle to pion K^+/π^+ , K^-/π^- , p/π^+ , and \bar{p}/π^- , are shown on figs. 5.14 to 5.16, as a function of x , at fixed values of the transverse momentum. For all ratios, data obtained with the “short” spectrometer have been plotted.

5.2. Cross sections as a function of the transverse momentum

The data at fixed values of the Feynman variable x or of the rapidity y_{lab} have been already published [8]. Examples of the invariant cross sections for the inclusive production of pions, kaons, and protons (antiprotons), as a function of the transverse momentum p_t , are presented in figs. 5.17 and 5.18 at a value of $x = 0.16$ and $y_{\text{lab}} = 1.5$, respectively.

Figs. 5.19 and 5.20 show the ratios of the invariant cross sections for particle to

Table 5.1

Table of the measured differential invariant cross sections $f = E(d^3\sigma/d^3p)$ as function of the longitudinal variables x and y_{lab} for fixed values of the transverse momentum p_t

\sqrt{s} (GeV)	p_t (GeV/c)	x	y_{lab}	π^+ (mb/GeV ² /c ³)	π^- (mb/GeV ² /c ³)
23.3	0.20	0.15	0.54	19.9 ± 2.9	13.9 ± 1.4
	0.22	0.16	0.53	21.0 ± 2.8	12.9 ± 1.3
	0.20	0.17	0.41	15.5 ± 1.7	10.6 ± 1.4
	0.22	0.19	0.40	14.6 ± 1.5	9.63 ± 1.20
	0.20	0.21	0.19	11.5 ± 1.3	
	0.23	0.23	0.20	10.4 ± 1.1	
	0.25	0.25	0.21	7.94 ± 0.87	
30.6	0.20	0.097	0.97	38.9 ± 5.8	21.2 ± 2.6
	0.22	0.11	0.94	31.8 ± 4.7	23.2 ± 2.6
	0.20	0.11	0.84	27.8 ± 3.2	19.8 ± 2.3
	0.22	0.12	0.83	23.3 ± 2.7	19.4 ± 2.1
	0.20	0.13	0.68	21.4 ± 1.6	16.5 ± 1.2
	0.22	0.14	0.68	19.3 ± 1.5	13.20 ± 0.97
	0.20	0.16	0.50	18.6 ± 1.8	12.30 ± 0.89
	0.22	0.17	0.51	16.0 ± 1.5	10.30 ± 0.74
	0.25	0.18	0.52	13.7 ± 1.3	8.68 ± 0.62
44.6	0.20	0.067	1.34	40.0 ± 4.0	30.5 ± 2.9
	0.22	0.072	1.32	40.5 ± 4.0	27.1 ± 2.6
	0.20	0.076	1.22	37.7 ± 4.8	30.9 ± 3.7
	0.22	0.082	1.20	35.5 ± 4.4	29.9 ± 3.5
	0.20	0.089	1.06	25.9 ± 2.4	22.3 ± 1.8
	0.22	0.096	1.05	26.3 ± 2.4	19.9 ± 1.6
	0.20	0.10	0.94	29.3 ± 2.7	21.5 ± 1.6
	0.22	0.11	0.95	28.6 ± 2.5	19.6 ± 1.5
	0.20	0.11	0.84	23.9 ± 1.9	19.4 ± 1.5
	0.23	0.12	0.85	20.6 ± 1.6	16.0 ± 1.2
	0.25	0.13	0.86	19.3 ± 1.5	13.8 ± 1.0
53.0	0.20	0.047	1.69	52.3 ± 5.6	44.1 ± 4.3
	0.21	0.051	1.66	48.6 ± 5.1	41.6 ± 4.0
	0.20	0.057	1.51	47.0 ± 4.6	41.0 ± 4.0
	0.22	0.061	1.49	46.1 ± 4.5	38.2 ± 3.7
	0.20	0.066	1.36	41.3 ± 4.2	32.3 ± 3.2
	0.22	0.071	1.34	41.1 ± 4.1	33.2 ± 3.3
	0.20	0.075	1.23	36.2 ± 3.2	28.0 ± 1.9
	0.20	0.077	1.21	39.0 ± 2.8	

Table 5.1 (continued)

\sqrt{s} (GeV)	P_t (GeV/c)	x	y_{lab}	π^+ (mb/GeV ² /c ³)		π^- (mb/GeV ² /c ³)	
	0.22	0.081	1.22	31.8	± 2.8	26.4	± 1.8
	0.22	0.083	1.20	34.0	± 2.4		
	0.20	0.085	1.11	33.4	± 2.7	23.4	± 2.0
	0.20	0.092	1.03	29.2	± 2.2		
	0.22	0.092	1.11	29.7	± 2.4	22.0	± 1.8
	0.20	0.094	1.00	31.4	± 2.6	20.9	± 1.5
	0.23	0.099	1.03	27.4	± 2.1		
	0.23	0.10	1.01	30.2	± 2.5	18.2	± 1.3
	0.25	0.11	1.05	25.5	± 1.9		
	0.25	0.11	1.03	26.1	± 2.1	16.4	± 1.1
62.7	0.20	0.063	1.40	54.8	± 7.6	27.2	± 3.4
	0.22	0.068	1.40	39.1	± 5.6	26.9	± 3.1
	0.24	0.073	1.39	35.0	± 4.9	27.0	± 2.9
23.3	0.40	0.17	0.95	6.65	± 1.20	4.58	± 0.82
	0.42	0.19	0.92	6.28	± 1.10		
	0.40	0.25	0.59	4.96	± 0.48	2.65	± 0.24
	0.40	0.26	0.55	4.64	± 0.56	3.08	± 0.30
	0.43	0.27	0.58	3.73	± 0.35	1.96	± 0.17
	0.43	0.28	0.54	2.84	± 0.37	2.32	± 0.23
	0.46	0.29	0.57	3.11	± 0.29	1.73	± 0.15
	0.46	0.30	0.54	3.14	± 0.39	1.68	± 0.17
30.6	0.40	0.13	1.23	8.88	± 0.93	7.18	± 0.61
	0.42	0.14	1.20	6.38	± 0.69	5.56	± 0.48
	0.40	0.16	1.05	8.12	± 0.72	5.64	± 0.40
	0.42	0.17	1.03	7.67	± 0.67	5.03	± 0.36
	0.40	0.20	0.83	6.32	± 0.49	4.25	± 0.32
	0.43	0.21	0.82	5.19	± 0.41	3.47	± 0.26
	0.40	0.26	0.54	4.14	± 0.59	2.59	± 0.20
	0.44	0.28	0.56	3.16	± 0.46	2.06	± 0.16
	0.40	0.29	0.43	5.02	± 0.62	2.02	± 0.23
	0.40	0.31	0.36	2.86	± 0.30	1.58	± 0.14
	0.45	0.32	0.45			1.38	± 0.16
	0.40	0.33	0.32	2.82	± 0.39	1.51	± 0.14
	0.45	0.34	0.39	2.31	± 0.25	1.09	± 0.10
	0.45	0.35	0.35	2.39	± 0.33	1.16	± 0.11
	0.50	0.36	0.42	1.67	± 0.19	0.779	± 0.073
	0.51	0.38	0.39	1.34	± 0.21	0.712	± 0.073

Table 5.1 (continued)

\sqrt{s} (GeV)	p_t (GeV/c)	x	y_{lab}	π^+ (mb/GeV ² /c ³)	π^- (mb/GeV ² /c ³)
44.6	0.40	0.075	1.77	14.1 ± 1.6	11.1 ± 1.3
	0.42	0.082	1.73	10.0 ± 1.2	9.00 ± 1.00
	0.40	0.089	1.61	9.13 ± 0.96	7.69 ± 0.70
	0.42	0.096	1.57	9.29 ± 0.95	7.04 ± 0.64
	0.40	0.11	1.39	10.6 ± 1.2	8.42 ± 0.67
	0.43	0.12	1.37	9.53 ± 1.10	7.18 ± 0.56
	0.40	0.13	1.24	9.54 ± 0.78	7.67 ± 0.56
	0.40	0.13	1.21	8.31 ± 0.63	5.89 ± 0.53
	0.43	0.14	1.23	8.73 ± 0.64	6.11 ± 0.40
	0.43	0.14	1.20	7.26 ± 0.55	4.81 ± 0.43
	0.40	0.15	1.08	8.83 ± 0.93	5.96 ± 0.60
	0.44	0.16	1.08	6.57 ± 0.70	5.17 ± 0.52
	0.40	0.18	0.92	6.08 ± 0.52	4.35 ± 0.38
	0.44	0.19	0.93	5.14 ± 0.44	3.59 ± 0.32
	0.45	0.24	0.73	2.95 ± 0.34	2.17 ± 0.27
	0.51	0.26	0.77	2.27 ± 0.26	1.53 ± 0.19
53.0	0.40	0.049	2.19	11.5 ± 1.5	11.2 ± 1.4
	0.41	0.053	2.14	9.96 ± 1.30	11.1 ± 1.3
	0.40	0.057	2.05	12.0 ± 1.5	11.9 ± 1.5
	0.40	0.058	2.02	15.8 ± 1.8	
	0.42	0.061	2.01	12.1 ± 1.5	10.1 ± 1.2
	0.42	0.063	1.98	14.2 ± 1.6	
	0.40	0.064	1.93	12.0 ± 1.3	10.9 ± 1.3
	0.42	0.069	1.89	11.2 ± 1.2	10.8 ± 1.3
	0.40	0.075	1.77	11.90 ± 0.83	10.20 ± 0.73
	0.40	0.082	1.69	12.8 ± 1.1	
	0.42	0.082	1.74	11.10 ± 0.76	8.84 ± 0.63
	0.42	0.089	1.66	11.30 ± 0.99	
	0.40	0.094	1.55	10.90 ± 0.86	10.30 ± 0.77
	0.43	0.10	1.53	10.30 ± 0.80	8.20 ± 0.61
	0.40	0.11	1.41	11.10 ± 0.86	9.13 ± 0.73
	0.40	0.11	1.37	10.20 ± 0.62	7.81 ± 0.52
	0.43	0.12	1.40	10.50 ± 0.72	8.08 ± 0.58
	0.43	0.12	1.36	9.53 ± 0.59	6.75 ± 0.45
	0.40	0.15	1.09	8.34 ± 0.51	5.95 ± 0.36
	0.40	0.16	1.03	7.56 ± 0.54	
	0.44	0.16	1.10	6.77 ± 0.42	4.75 ± 0.29
	0.44	0.17	1.04	6.41 ± 0.45	

Table 5.1 (continued)

\sqrt{s} (GeV)	p_t (GeV/c)	x	y_{lab}	π^+ (mb/GeV ² /c ³)	π^- (mb/GeV ² /c ³)
62.7	0.40	0.19	0.86	6.59 \pm 0.41	3.96 \pm 0.26
	0.45	0.20	0.90	5.33 \pm 0.33	3.16 \pm 0.21
	0.51	0.22	0.93	4.11 \pm 0.26	2.31 \pm 0.15
	0.40	0.091	1.59	11.5 \pm 2.2	7.97 \pm 0.62
	0.43	0.098	1.57	8.85 \pm 1.70	7.16 \pm 0.50
	0.46	0.11	1.56	6.60 \pm 1.30	5.75 \pm 0.41
	0.80	0.50	0.55	0.247 \pm 0.022	0.0650 \pm 0.0110
	0.86	0.53	0.54	0.136 \pm 0.014	0.0436 \pm 0.0079
	0.92	0.57	0.53	0.0681 \pm 0.0083	0.0155 \pm 0.0043
30.6	0.80	0.31	1.03	0.595 \pm 0.052	0.250 \pm 0.032
	0.85	0.33	1.01	0.475 \pm 0.042	0.225 \pm 0.028
	0.80	0.38	0.82	0.319 \pm 0.053	0.221 \pm 0.025
	0.80	0.39	0.79	0.416 \pm 0.041	0.204 \pm 0.021
	0.86	0.41	0.82	0.323 \pm 0.050	0.106 \pm 0.015
	0.86	0.42	0.78	0.251 \pm 0.028	0.128 \pm 0.015
	0.80	0.47	0.61	0.216 \pm 0.023	
	0.87	0.51	0.62	0.115 \pm 0.014	
	0.80	0.53	0.48	0.154 \pm 0.028	
	0.88	0.57	0.50	0.0728 \pm 0.0170	
	0.97	0.61	0.53	0.0266 \pm 0.0095	
	0.80	0.15	1.72	0.768 \pm 0.130	0.759 \pm 0.093
44.6	0.83	0.16	1.69	0.721 \pm 0.120	0.654 \pm 0.080
	0.80	0.18	1.57	0.690 \pm 0.069	0.544 \pm 0.041
	0.84	0.19	1.54	0.683 \pm 0.065	0.412 \pm 0.032
	0.80	0.22	1.35	0.716 \pm 0.064	0.475 \pm 0.042
	0.85	0.24	1.33	0.499 \pm 0.047	0.370 \pm 0.033
	0.80	0.26	1.20	0.727 \pm 0.061	0.423 \pm 0.030
	0.80	0.27	1.17	0.655 \pm 0.056	0.353 \pm 0.029
	0.86	0.28	1.19	0.457 \pm 0.042	0.299 \pm 0.022
	0.86	0.29	1.16	0.430 \pm 0.039	0.241 \pm 0.020
	0.80	0.30	1.04	0.526 \pm 0.079	0.346 \pm 0.024
	0.87	0.33	1.05	0.400 \pm 0.063	0.223 \pm 0.017
	0.80	0.36	0.88	0.414 \pm 0.034	0.240 \pm 0.019
	0.88	0.38	0.90	0.260 \pm 0.023	0.128 \pm 0.011
	0.97	0.41	0.92	0.128 \pm 0.013	0.0687 \pm 0.0071

Table 5.1 (continued)

\sqrt{s} (GeV)	p_t (GeV/c)	x	y_{lab}	π^+ (mb/GeV ² /c ³)	π^- (mb/GeV ² /c ³)
53.0	0.80	0.11	2.03	1.17 \pm 0.10	
	0.80	0.11	2.01	1.02 \pm 0.15	0.893 \pm 0.084
	0.83	0.12	1.98	1.130 \pm 0.095	
	0.83	0.12	1.97	1.02 \pm 0.14	0.746 \pm 0.070
	0.80	0.13	1.86	0.900 \pm 0.100	0.732 \pm 0.068
	0.84	0.14	1.82	0.784 \pm 0.090	0.626 \pm 0.058
	0.80	0.15	1.73	0.911 \pm 0.073	0.656 \pm 0.047
	0.84	0.16	1.70	0.694 \pm 0.057	0.507 \pm 0.037
	0.80	0.17	1.61	0.890 \pm 0.100	0.712 \pm 0.065
	0.85	0.18	1.59	0.667 \pm 0.080	0.517 \pm 0.049
	0.80	0.19	1.51	0.878 \pm 0.070	0.579 \pm 0.054
	0.85	0.20	1.49	0.693 \pm 0.056	0.455 \pm 0.043
	0.80	0.22	1.36	0.743 \pm 0.063	0.506 \pm 0.040
	0.80	0.23	1.33	0.804 \pm 0.086	0.520 \pm 0.042
	0.86	0.24	1.36	0.563 \pm 0.049	0.388 \pm 0.032
	0.86	0.25	1.32	0.561 \pm 0.064	0.323 \pm 0.028
	0.80	0.26	1.18	0.615 \pm 0.065	0.472 \pm 0.033
	0.80	0.28	1.11	0.623 \pm 0.051	
	0.87	0.29	1.18	0.417 \pm 0.048	0.282 \pm 0.021
	0.80	0.30	1.04	0.568 \pm 0.047	0.341 \pm 0.023
	0.88	0.30	1.13	0.425 \pm 0.037	
	0.80	0.31	1.03	0.600 \pm 0.047	
	0.88	0.33	1.06	0.355 \pm 0.032	0.198 \pm 0.014
	0.88	0.33	1.05	0.310 \pm 0.028	
	0.97	0.35	1.08	0.203 \pm 0.021	0.1080 \pm 0.0082
	0.97	0.36	1.07	0.160 \pm 0.017	
62.7	0.80	0.18	1.54	0.896 \pm 0.093	0.607 \pm 0.049
	0.86	0.20	1.54	0.534 \pm 0.063	0.444 \pm 0.037
	0.92	0.21	1.53	0.428 \pm 0.052	0.347 \pm 0.030
30.6	1.20	0.47	1.00	0.0247 \pm 0.0065	
	1.27	0.51	0.98	0.0140 \pm 0.0045	
	1.20	0.56	0.81	0.0147 \pm 0.0034	
	1.29	0.61	0.81	0.0063 \pm 0.0020	
44.6	1.20	0.30	1.43	0.0706 \pm 0.0093	0.0449 \pm 0.0049
	1.27	0.33	1.41	0.0330 \pm 0.0054	0.0215 \pm 0.0029
	1.20	0.39	1.19	0.0406 \pm 0.0035	0.0269 \pm 0.0025
	1.29	0.42	1.19	0.0228 \pm 0.0022	0.0126 \pm 0.0014
	1.38	0.45	1.18	0.0117 \pm 0.0014	0.00570 \pm 0.00085

Table 5.1 (continued)

\sqrt{s} (GeV)	p_t (GeV/c)	x	y_{lab}	π^+ (mb/GeV ² /c ³)	π^- (mb/GeV ² /c ³)
53.0	1.20	0.23	1.72	0.0707 ± 0.0086	0.0536 ± 0.0055
	1.26	0.25	1.69	0.0584 ± 0.0072	0.0377 ± 0.0042
	1.20	0.26	1.57	0.0818 ± 0.0093	0.0419 ± 0.0041
	1.27	0.29	1.55	0.0470 ± 0.0062	0.0302 ± 0.0031
	1.20	0.30	1.44	0.0747 ± 0.0081	0.0422 ± 0.0034
	1.20	0.33	1.36	0.0610 ± 0.0066	0.0389 ± 0.0034
	1.28	0.33	1.43	0.0335 ± 0.0045	0.0269 ± 0.0024
	1.20	0.34	1.32	0.0632 ± 0.0077	0.0343 ± 0.0028
	1.20	0.35	1.30	0.0619 ± 0.0061	
	1.29	0.35	1.35	0.0299 ± 0.0040	0.0222 ± 0.0022
	1.29	0.37	1.32	0.0306 ± 0.0046	0.0188 ± 0.0018
	1.29	0.38	1.30	0.0330 ± 0.0038	
	1.38	0.38	1.34	0.0202 ± 0.0030	0.0135 ± 0.0015
	1.38	0.39	1.31	0.0215 ± 0.0036	0.00840 ± 0.00099
	1.39	0.40	1.29	0.0205 ± 0.0027	
\sqrt{s} (GeV)	p_t (GeV/c)	x	y_{lab}	K^+ (mb/GeV ² /c ³)	K^- (mb/GeV ² /c ³)
23.3	0.21	0.18	1.13	2.35 ± 0.52	0.653 ± 0.280
	0.21	0.23	0.91	0.964 ± 0.250	
30.6	0.21	0.14	1.40	1.76 ± 0.31	1.09 ± 0.19
	0.21	0.17	1.23	1.52 ± 0.28	0.741 ± 0.100
44.6	0.21	0.094	1.78	2.56 ± 0.56	1.94 ± 0.31
	0.21	0.11	1.67	3.37 ± 0.68	1.65 ± 0.25
	0.21	0.12	1.57	2.09 ± 0.32	0.951 ± 0.140
53.0	0.21	0.080	1.94	4.16 ± 0.83	1.80 ± 0.25
	0.21	0.082	1.92	3.04 ± 0.41	
	0.21	0.090	1.83	2.87 ± 0.45	1.79 ± 0.32
	0.21	0.098	1.75	2.58 ± 0.42	
	0.21	0.10	1.73	2.66 ± 0.38	1.32 ± 0.21
62.7	0.21	0.067	2.12	6.31 ± 2.10	
23.3	0.41	0.18	1.30	1.17 ± 0.41	
	0.42	0.26	0.95	0.667 ± 0.110	0.202 ± 0.041
	0.42	0.27	0.92	0.518 ± 0.120	0.157 ± 0.040

Table 5.1 (continued)

\sqrt{s} (GeV)	p_t (GeV/c)	x	y_{lab}	K^+ (mb/GeV ² /c ³)	K^- (mb/GeV ² /c ³)
30.6	0.41	0.14	1.57	1.10 \pm 0.25	0.706 \pm 0.150
	0.41	0.17	1.40	0.974 \pm 0.180	0.438 \pm 0.063
	0.42	0.21	1.19	1.01 \pm 0.13	0.289 \pm 0.050
	0.43	0.28	0.92	0.465 \pm 0.120	0.143 \pm 0.024
	0.43	0.31	0.80	0.376 \pm 0.086	0.0868 \pm 0.0210
	0.43	0.33	0.74	0.334 \pm 0.057	0.0823 \pm 0.0130
	0.44	0.34	0.70	0.293 \pm 0.070	0.0576 \pm 0.0120
44.6	0.41	0.094	1.95	1.04 \pm 0.20	0.816 \pm 0.130
	0.41	0.12	1.74	1.47 \pm 0.29	0.724 \pm 0.120
	0.42	0.14	1.60	0.897 \pm 0.130	0.529 \pm 0.073
	0.42	0.14	1.57	0.882 \pm 0.110	0.484 \pm 0.074
	0.42	0.16	1.45	1.06 \pm 0.15	0.460 \pm 0.066
	0.43	0.19	1.29	0.642 \pm 0.083	0.328 \pm 0.045
	0.44	0.24	1.08	0.426 \pm 0.073	0.143 \pm 0.028
53.0	0.41	0.080	2.11	1.18 \pm 0.16	1.04 \pm 0.12
	0.41	0.087	2.04	1.10 \pm 0.23	
	0.41	0.10	1.90	1.71 \pm 0.24	0.864 \pm 0.120
	0.42	0.12	1.77	1.27 \pm 0.15	0.748 \pm 0.110
	0.42	0.12	1.73	1.20 \pm 0.10	0.646 \pm 0.076
	0.43	0.16	1.46	0.869 \pm 0.075	0.435 \pm 0.042
	0.43	0.17	1.40	0.811 \pm 0.093	
	0.44	0.20	1.25	0.713 \pm 0.059	0.314 \pm 0.031
62.7	0.42	0.097	1.95		0.597 \pm 0.088
23.3	0.84	0.53	0.67	0.0479 \pm 0.0060	0.0469 \pm 0.0190
30.6	0.83	0.32	1.14	0.0832 \pm 0.0120	0.0318 \pm 0.0080
	0.84	0.40	0.95	0.0616 \pm 0.0160	0.0164 \pm 0.0044
	0.84	0.41	0.91	0.0468 \pm 0.0085	0.00733 \pm 0.00240
	0.85	0.50	0.74	0.0293 \pm 0.0054	
44.6	0.82	0.16	1.83		0.0972 \pm 0.0250
	0.83	0.19	1.67	0.157 \pm 0.022	0.0720 \pm 0.0092
	0.84	0.24	1.46	0.103 \pm 0.014	0.0405 \pm 0.0067
	0.84	0.27	1.33	0.127 \pm 0.016	0.0347 \pm 0.0045
	0.84	0.28	1.29	0.0872 \pm 0.0011	0.0279 \pm 0.0041
	0.85	0.32	1.17		0.0193 \pm 0.0027
	0.86	0.38	1.02	0.0426 \pm 0.0059	0.0150 \pm 0.0025

Table 5.1 (continued)

\sqrt{s} (GeV)	p_t (GeV/c)	x	y_{lab}	K^+ (mb/GeV ² /c ³)	K^- (mb/GeV ² /c ³)
53.0	0.82	0.12	2.12	0.296 \pm 0.038	
	0.82	0.12	2.11	0.319 \pm 0.066	0.118 \pm 0.021
	0.82	0.14	1.96	0.218 \pm 0.037	0.110 \pm 0.017
	0.83	0.16	1.84	0.150 \pm 0.017	0.0784 \pm 0.0090
	0.83	0.18	1.73	0.194 \pm 0.032	0.0762 \pm 0.0130
	0.84	0.20	1.63	0.115 \pm 0.014	0.0554 \pm 0.0096
	0.84	0.23	1.49	0.133 \pm 0.016	0.0507 \pm 0.0071
	0.84	0.24	1.46	0.155 \pm 0.024	0.0355 \pm 0.0056
	0.85	0.28	1.31	0.104 \pm 0.017	0.0312 \pm 0.0036
	0.86	0.30	1.25	0.0953 \pm 0.0120	
	0.86	0.32	1.18	0.0784 \pm 0.0099	0.0272 \pm 0.0029
	0.86	0.33	1.17	0.0876 \pm 0.0100	
62.7	0.84	0.19	1.67	0.191 \pm 0.028	0.0738 \pm 0.0099
30.6	1.25	0.50	1.05	0.00493 \pm 0.00200	
	1.27	0.60	0.87	0.00369 \pm 0.00120	
44.6	1.25	0.32	1.48	0.0116 \pm 0.0024	0.00429 \pm 0.00100
	1.27	0.41	1.25	0.00881 \pm 0.00110	0.00170 \pm 0.00037
53.0	1.24	0.24	1.76	0.0275 \pm 0.0040	0.00943 \pm 0.00160
	1.25	0.28	1.62	0.0178 \pm 0.0029	0.00505 \pm 0.00090
	1.26	0.32	1.49	0.0190 \pm 0.0028	0.00435 \pm 0.00066
	1.27	0.35	1.41	0.0118 \pm 0.0019	0.00413 \pm 0.00066
	1.27	0.36	1.38	0.0154 \pm 0.0025	0.00229 \pm 0.00040
	1.27	0.37	1.36	0.00997 \pm 0.00160	
\sqrt{s} (GeV)	p_t (GeV/c)	x	y_{lab}	p (mb/GeV ² /c ³)	\bar{p} (mb/GeV ² /c ³)
23.3	0.17	0.15	1.84	6.40 \pm 1.40	
	0.19	0.16	1.78	4.30 \pm 1.00	0.480 \pm 0.110
	0.17	0.17	1.72	5.04 \pm 0.85	
	0.20	0.19	1.66	5.28 \pm 0.80	
	0.18	0.21	1.52	4.54 \pm 0.73	
	0.21	0.23	1.45	5.19 \pm 0.72	
	0.24	0.25	1.39	4.57 \pm 0.62	

Table 5.1 (continued)

\sqrt{s} (GeV)	p_t (GeV/c)	x	y_{lab}	P (mb/GeV ² /c ³)		\bar{P} (mb/GeV ² /c ³)	
30.6	0.18	0.11	2.19			1.03	± 0.15
	0.17	0.11	2.14	2.62	± 0.71		
	0.19	0.12	2.08	3.26	± 0.73	0.854	± 0.150
	0.17	0.13	2.00	3.14	± 0.42		
	0.20	0.14	1.93	3.38	± 0.40	0.502	± 0.073
	0.18	0.16	1.83	4.88	± 0.65		
	0.20	0.17	1.77	4.87	± 0.61	0.396	± 0.047
	0.23	0.18	1.71	4.91	± 0.58		
44.6	0.17	0.067	2.63	2.44	± 0.53		
	0.18	0.072	2.57	3.53	± 0.61	1.06	± 0.13
	0.17	0.076	2.52	3.97	± 0.86		
	0.19	0.082	2.46	3.00	± 0.67	0.985	± 0.130
	0.17	0.089	2.38	3.07	± 0.60		
	0.20	0.096	2.31	3.21	± 0.57	0.683	± 0.099
	0.18	0.10	2.27	3.26	± 0.66		
	0.18	0.11	2.17	3.13	± 0.40		
	0.20	0.11	2.20	3.09	± 0.59	0.722	± 0.097
	0.21	0.12	2.11	3.86	± 0.42	0.693	± 0.082
	0.24	0.13	2.05	3.02	± 0.34		
53.0	0.16	0.047	2.94	2.70	± 0.79		
	0.18	0.051	2.88	1.88	± 0.57	1.13	± 0.14
	0.17	0.057	2.79	2.50	± 0.51		
	0.18	0.061	2.73	2.48	± 0.46	1.23	± 0.14
	0.17	0.066	2.66	3.82	± 0.70		
	0.19	0.071	2.59	2.39	± 0.49	1.18	± 0.14
	0.17	0.075	2.54	2.94	± 0.63		
	0.17	0.077	2.52	2.51	± 0.30		
	0.20	0.081	2.48	3.29	± 0.63	0.949	± 0.100
	0.20	0.083	2.46	3.04	± 0.32		
	0.18	0.085	2.43	2.52	± 0.38		
	0.18	0.092	2.36	3.33	± 0.48		
	0.20	0.092	2.37	2.82	± 0.38	0.883	± 0.140
	0.18	0.094	2.34	4.58	± 0.50		
	0.21	0.099	2.29	3.17	± 0.43	0.833	± 0.110
	0.21	0.10	2.27	3.51	± 0.39		
	0.23	0.11	2.23	2.61	± 0.35		
	0.23	0.11	2.21	3.58	± 0.38		

Table 5.1 (continued)

\sqrt{s} (GeV)	p_t (GeV/c)	x	y_{lab}	P (mb/GeV ² /c ³)	\bar{P} (mb/GeV ² /c ³)
23.3	0.37	0.17	1.78	3.86 ± 0.90	
	0.40	0.19	1.71	3.51 ± 0.78	
	0.38	0.25	1.44	4.20 ± 0.43	
	0.38	0.26	1.40	4.90 ± 0.62	
	0.41	0.27	1.38	3.96 ± 0.39	0.0693 ± 0.0166
	0.41	0.28	1.34	5.11 ± 0.61	0.0846 ± 0.0222
	0.44	0.29	1.32	4.34 ± 0.40	
	0.45	0.30	1.29	5.17 ± 0.59	
30.6	0.37	0.13	2.05	2.22 ± 0.38	
	0.40	0.14	1.99	1.88 ± 0.32	0.308 ± 0.055
	0.38	0.16	1.89	2.56 ± 0.34	
	0.40	0.17	1.82	2.48 ± 0.30	0.274 ± 0.031
	0.38	0.20	1.68	2.85 ± 0.31	
	0.41	0.21	1.62	3.26 ± 0.32	0.176 ± 0.029
	0.39	0.26	1.40	3.84 ± 0.60	
	0.43	0.28	1.35	4.82 ± 0.67	0.0660 ± 0.0130
	0.39	0.29	1.29	6.82 ± 0.85	
	0.39	0.31	1.23	4.31 ± 0.45	0.0643 ± 0.0160
	0.39	0.33	1.19	5.97 ± 0.75	
	0.44	0.34	1.17	4.19 ± 0.43	0.0339 ± 0.0068
	0.44	0.35	1.13	4.84 ± 0.61	0.0282 ± 0.0080
	0.49	0.36	1.12	4.48 ± 0.44	
	0.50	0.38	1.09	4.63 ± 0.57	
44.6	0.37	0.075	2.57	1.99 ± 0.46	
	0.39	0.082	2.51	1.62 ± 0.37	0.422 ± 0.110
	0.37	0.089	2.43	1.70 ± 0.27	
	0.40	0.096	2.37	1.45 ± 0.23	0.387 ± 0.052
	0.38	0.11	2.23	2.08 ± 0.37	
	0.41	0.12	2.16	2.48 ± 0.39	0.417 ± 0.055
	0.38	0.13	2.09	2.09 ± 0.26	
	0.38	0.13	2.06	1.99 ± 0.22	
	0.41	0.14	2.03	1.98 ± 0.23	0.386 ± 0.045
	0.41	0.14	2.00	1.93 ± 0.20	0.275 ± 0.040
	0.38	0.15	1.94	2.56 ± 0.34	
	0.42	0.16	1.88	2.43 ± 0.32	0.294 ± 0.041
	0.39	0.18	1.78	2.66 ± 0.28	
	0.43	0.19	1.72	2.73 ± 0.28	0.174 ± 0.025

Table 5.1 (continued)

\sqrt{s} (GeV)	p_t (GeV/c)	x	y_{lab}	P (mb/GeV ² /c ³)	\bar{P} (mb/GeV ² /c ³)
53.0	0.44	0.24	1.51	2.49 ± 0.31	0.0907 ± 0.0190
	0.50	0.26	1.47	2.60 ± 0.32	
	0.36	0.049	2.96	1.72 ± 0.34	0.472 ± 0.120
	0.38	0.053	2.89	1.36 ± 0.26	
	0.37	0.058	2.82	1.40 ± 0.38	0.621 ± 0.100
	0.39	0.061	2.78	1.89 ± 0.34	
	0.37	0.064	2.73	2.39 ± 0.37	0.538 ± 0.100
	0.39	0.069	2.67	2.01 ± 0.31	
	0.37	0.075	2.59	1.84 ± 0.17	0.568 ± 0.053
	0.38	0.082	2.52	1.85 ± 0.31	
	0.40	0.082	2.53	1.65 ± 0.15	0.565 ± 0.062
	0.40	0.089	2.46	1.46 ± 0.25	
	0.38	0.094	2.39	2.01 ± 0.24	0.550 ± 0.073
	0.41	0.10	2.33	1.88 ± 0.22	
	0.38	0.11	2.26	2.33 ± 0.26	0.444 ± 0.047
	0.38	0.11	2.22	1.91 ± 0.16	
	0.41	0.12	2.19	2.42 ± 0.25	0.353 ± 0.032
	0.41	0.12	2.16	1.98 ± 0.17	
	0.39	0.15	1.95	2.31 ± 0.19	0.181 ± 0.019
	0.39	0.16	1.89	2.60 ± 0.26	
62.7	0.43	0.16	1.89	2.28 ± 0.18	0.605 ± 0.074
	0.43	0.17	1.83	2.41 ± 0.23	
	0.39	0.19	1.73	2.93 ± 0.22	
23.3	0.44	0.20	1.68	3.06 ± 0.23	0.145 ± 0.045
	0.50	0.22	1.63	2.71 ± 0.20	
	0.38	0.091	2.43	1.64 ± 0.83	
30.6	0.44	0.11	2.32	1.36 ± 0.61	0.0796 ± 0.0270
	0.79	0.50	0.95	1.49 ± 0.11	
	0.85	0.53	0.91	1.250 ± 0.091	
30.6	0.91	0.57	0.87	0.818 ± 0.061	0.0434 ± 0.0180
	0.79	0.31	1.43	0.902 ± 0.077	
	0.84	0.33	1.38	0.786 ± 0.067	
	0.79	0.38	1.23	1.11 ± 0.12	
	0.79	0.39	1.19	1.29 ± 0.11	
30.6	0.85	0.41	1.18	0.945 ± 0.110	0.0796 ± 0.0270
	0.85	0.42	1.15	1.010 ± 0.084	

Table 5.1 (continued)

\sqrt{s} (GeV)	p_t (GeV/c)	x	y_{lab}	P (mb/GeV ² /c ³)	\bar{P} (mb/GeV ² /c ³)
44.6	0.79	0.47	1.02	1.260 \pm 0.095	
	0.87	0.51	0.98	0.951 \pm 0.072	
	0.79	0.53	0.89	1.31 \pm 0.12	
	0.88	0.57	0.86	0.865 \pm 0.084	
	0.97	0.61	0.84	0.481 \pm 0.053	
	0.78	0.15	2.12	0.345 \pm 0.089	
	0.82	0.16	2.06	0.439 \pm 0.094	0.0638 \pm 0.0150
	0.79	0.18	1.96	0.531 \pm 0.061	
	0.83	0.19	1.91	0.458 \pm 0.053	0.0443 \pm 0.0057
	0.79	0.22	1.75	0.644 \pm 0.064	
	0.84	0.24	1.70	0.527 \pm 0.053	0.0242 \pm 0.0044
	0.79	0.26	1.61	0.808 \pm 0.072	
	0.79	0.27	1.57	0.734 \pm 0.067	
	0.85	0.28	1.56	0.719 \pm 0.064	0.0178 \pm 0.0026
	0.85	0.29	1.53	0.613 \pm 0.056	0.0161 \pm 0.0026
	0.79	0.30	1.45	1.09 \pm 0.14	
	0.86	0.33	1.41	0.926 \pm 0.120	0.0125 \pm 0.0019
	0.79	0.36	1.29	0.942 \pm 0.076	
	0.88	0.38	1.26	0.654 \pm 0.054	0.00633 \pm 0.00130
	0.96	0.41	1.23	0.437 \pm 0.037	
	0.78	0.11	2.41	0.461 \pm 0.058	
	0.78	0.11	2.40	0.343 \pm 0.083	
	0.81	0.12	2.35	0.454 \pm 0.054	0.0987 \pm 0.0140
	0.81	0.12	2.34	0.490 \pm 0.094	
	0.78	0.13	2.25	0.458 \pm 0.072	
	0.82	0.14	2.20	0.427 \pm 0.065	0.0728 \pm 0.0110
	0.79	0.15	2.13	0.493 \pm 0.049	
	0.83	0.16	2.07	0.422 \pm 0.042	0.0661 \pm 0.0069
	0.79	0.17	2.01	0.525 \pm 0.078	
	0.84	0.18	1.96	0.490 \pm 0.070	0.0575 \pm 0.0090
	0.79	0.19	1.91	0.564 \pm 0.054	
	0.84	0.20	1.86	0.545 \pm 0.050	0.0414 \pm 0.0071
	0.79	0.22	1.77	0.632 \pm 0.061	
	0.79	0.23	1.74	0.629 \pm 0.078	
	0.85	0.24	1.73	0.580 \pm 0.055	0.0421 \pm 0.0056
	0.85	0.25	1.69	0.647 \pm 0.076	0.0275 \pm 0.0042
	0.79	0.26	1.59	0.874 \pm 0.091	

Table 5.1 (continued)

\sqrt{s} (GeV)	p_t (GeV/c)	x	y_{lab}	p (mb/GeV ² /c ³)	\bar{p} (mb/GeV ² /c ³)
	0.79	0.28	1.52	0.830 \pm 0.071	0.0194 \pm 0.0023
	0.87	0.29	1.55	0.714 \pm 0.075	
	0.79	0.30	1.45	0.955 \pm 0.080	
	0.87	0.30	1.49	0.683 \pm 0.058	0.0130 \pm 0.0016
	0.79	0.31	1.44	0.826 \pm 0.068	
	0.88	0.33	1.42	0.740 \pm 0.063	
	0.88	0.33	1.41	0.614 \pm 0.051	
	0.96	0.35	1.40	0.485 \pm 0.043	
	0.97	0.36	1.38	0.411 \pm 0.036	
62.7	0.79	0.18	1.95	0.663 \pm 0.085	0.0671 \pm 0.0083
	0.85	0.20	1.91	0.588 \pm 0.073	
	0.91	0.21	1.87	0.440 \pm 0.057	
30.6	1.19	0.47	1.22	0.107 \pm 0.016	
	1.27	0.51	1.18	0.0952 \pm 0.0140	
	1.19	0.56	1.04	0.152 \pm 0.015	
	1.28	0.61	1.01	0.0779 \pm 0.0090	
44.6	1.19	0.30	1.66	0.104 \pm 0.013	0.00192 \pm 0.00054
	1.26	0.33	1.62	0.0837 \pm 0.0110	
	1.19	0.39	1.42	0.1080 \pm 0.0083	0.00059 \pm 0.00018
	1.28	0.42	1.39	0.0749 \pm 0.0059	
	1.37	0.45	1.36	0.0437 \pm 0.0038	
53.0	1.19	0.23	1.94	0.0844 \pm 0.0110	0.00409 \pm 0.00085
	1.25	0.25	1.90	0.0565 \pm 0.0075	
	1.19	0.26	1.79	0.0997 \pm 0.0120	
	1.26	0.29	1.75	0.0627 \pm 0.0080	0.00278 \pm 0.00056
	1.19	0.30	1.66	0.116 \pm 0.012	
	1.19	0.33	1.58	0.118 \pm 0.011	0.00249 \pm 0.00041
	1.28	0.33	1.63	0.0794 \pm 0.0085	
	1.19	0.34	1.55	0.133 \pm 0.014	
	1.19	0.35	1.52	0.130 \pm 0.011	0.00152 \pm 0.00029
	1.28	0.35	1.55	0.0728 \pm 0.0076	
	1.29	0.37	1.52	0.0778 \pm 0.0089	
	1.29	0.38	1.50	0.0719 \pm 0.0070	
	1.37	0.38	1.52	0.0486 \pm 0.0055	
	1.38	0.39	1.49	0.0561 \pm 0.0068	
	1.38	0.40	1.47	0.0412 \pm 0.0045	

The errors quoted include statistical uncertainties as well as uncertainties arising from the corrections and the luminosity determinations. An energy-dependent scale error estimated to be at most 5% may be present.

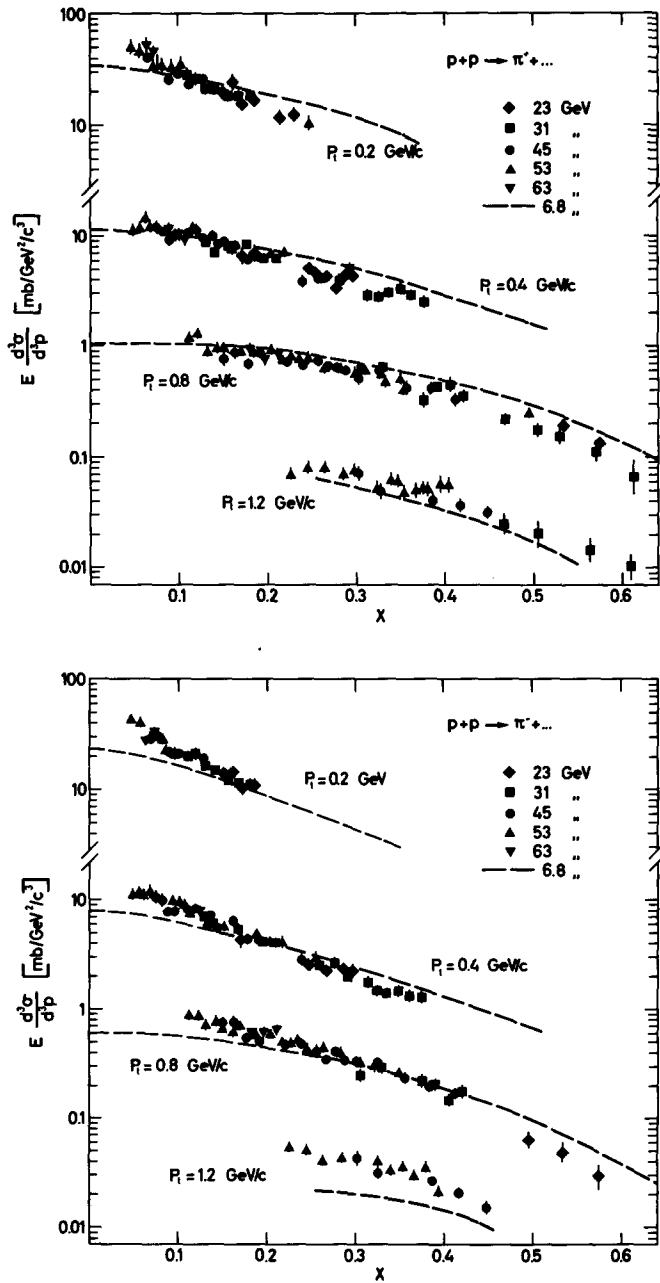


Fig. 5.1. The invariant cross sections for the inclusive production of π^+ and π^- versus the x variable at fixed values of p_T . The dashed lines represent interpolations of the 24 GeV/c data (refs. [19, 20]).

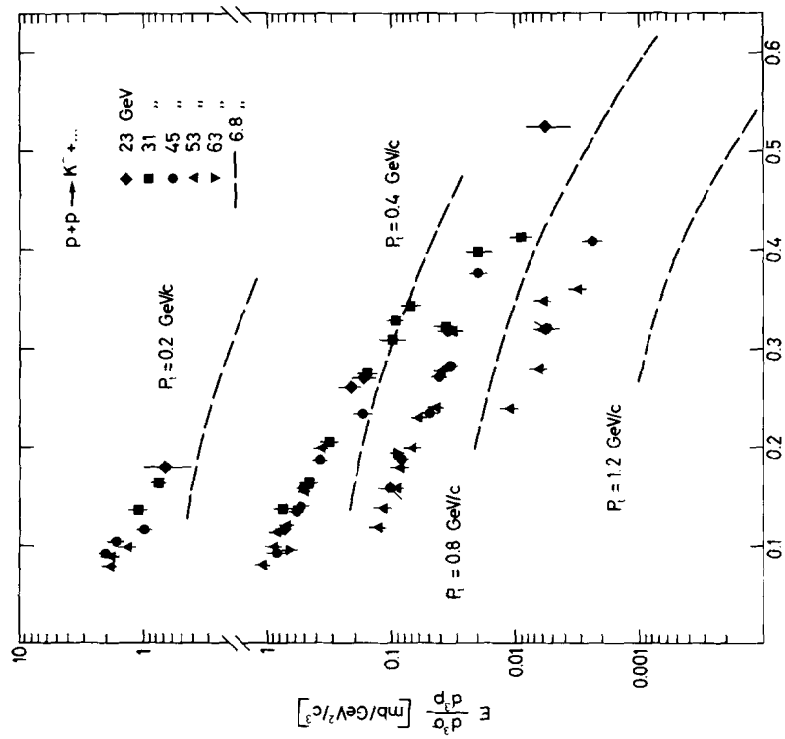


Fig. 5.3. The invariant cross sections for K^- production versus x at fixed values of P_T .

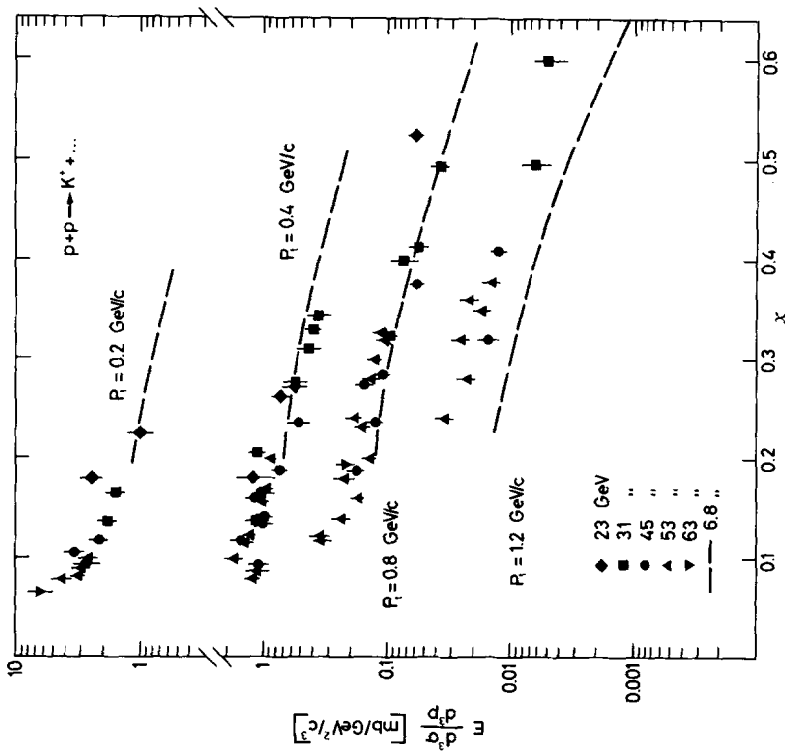


Fig. 5.2. The invariant cross sections for K^+ production versus x at fixed values of P_T .

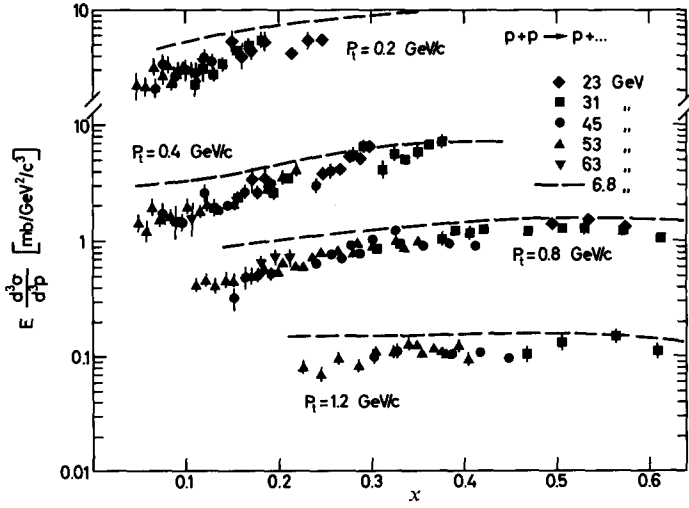


Fig. 5.4. The invariant cross sections for proton production *versus* x at fixed values of p_T .

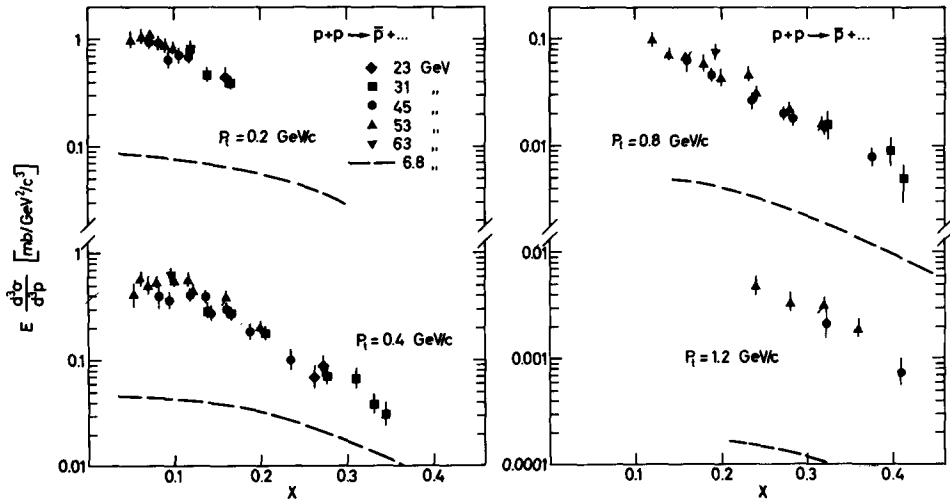


Fig. 5.5. The invariant cross sections for antiproton production *versus* x at fixed values of p_T .

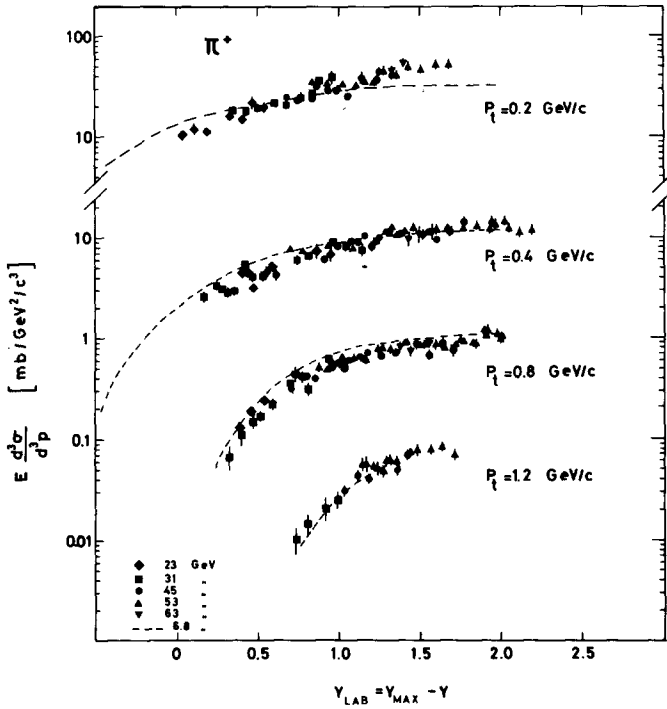


Fig. 5.6. The invariant cross sections for π^+ production versus y_{lab} at fixed values of p_t .

antiparticle π^+/π^- , K^+/K^- , and p/\bar{p} , and for particle to pion K^+/π^+ , K^-/π^- , p/π^+ , and \bar{p}/π^- , as a function of p_t , at a value of $x = 0.16$ and $y_{lab} = 1.5$, respectively.

6. Discussion

The measured invariant cross sections will now be discussed in terms of their dependence on the longitudinal variables (x and y_{lab}), on the transverse momentum, and on energy.

6.1. Dependence on x and on y_{lab}

As shown in fig. 5.1 the invariant cross sections for pions, at fixed p_t , decrease with increasing x . The decrease is faster than an exponential; it may be approximated with a Gaussian form in x or, better, with a quadratic exponential form. In the range

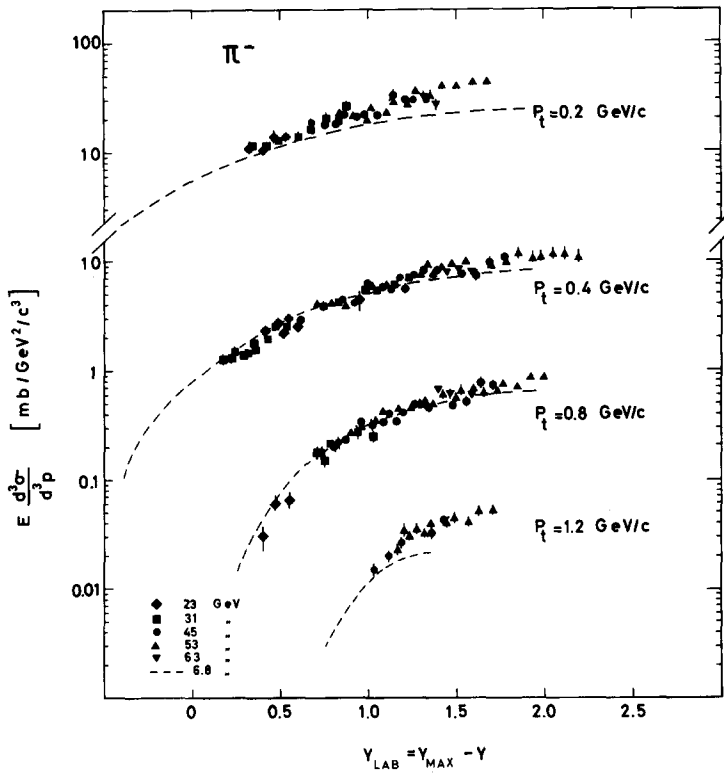


Fig. 5.7. The invariant cross sections for π^- production versus y_{lab} at fixed values of p_t .

explored in this experiment, the slopes of the distributions depend on the value of p_t , being steeper for smaller values of the transverse momentum. Furthermore, the decrease of the invariant cross section with x is more pronounced for π^- than for π^+ production.

The x distributions for K^+ , K^- , and \bar{p} production have the same qualitative behaviour as for pions (figs. 5.2, 5.3 and 5.5). In particular it seems that the slope of the x distribution for K^- is steeper than that for K^+ , at every value of p_t . This feature of pion and kaon production is more evident when considering the ratios of the invariant cross sections for particle and antiparticle production (fig. 5.12). These ratios decrease towards 1, going from the fragmentation to the central region (that is, when x goes to 0).

The x dependence of the invariant cross sections for protons is completely different from that of the other particles. The fact that the cross section increases with x (fig. 5.4) is a consequence of the "leading" particle nature of the proton.

The dependences on the laboratory rapidity of the invariant cross sections for pi-

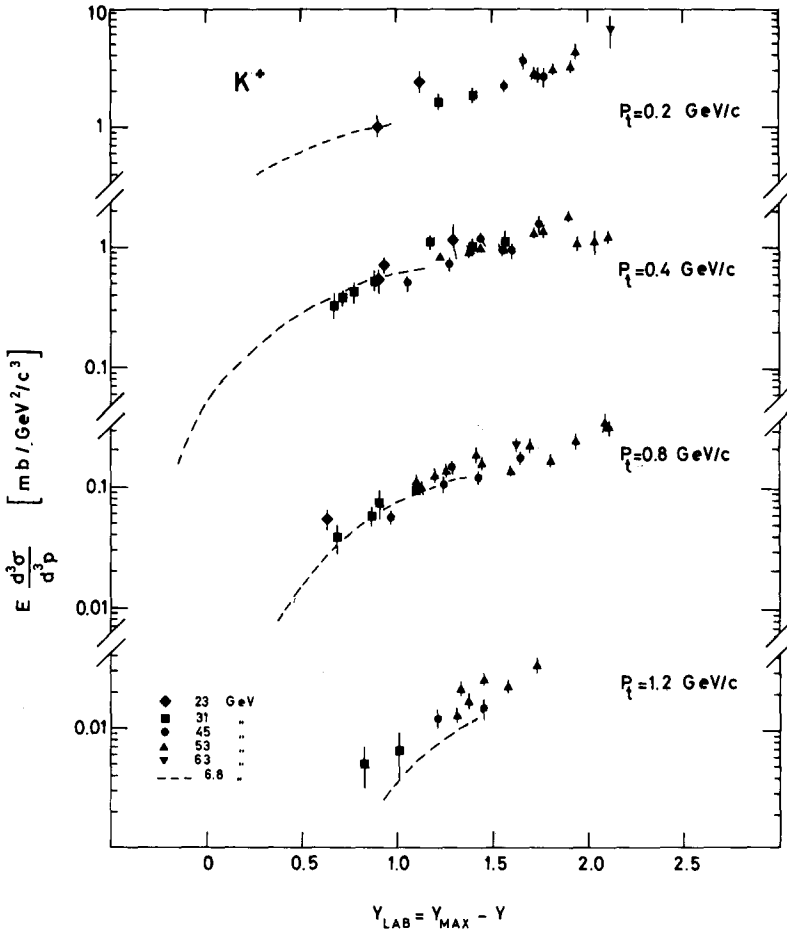


Fig. 5.8. The invariant cross sections for K^+ production versus y_{lab} at fixed values of p_t .

ons, kaons, and antiprotons, at fixed p_t values, are quite similar and may be discussed at the same time. Fig. 6.1 presents a compilation of the data obtained at $p_t = 0.4$ GeV/c in different ISR experiments [21–23]. The cross sections increase rapidly until $y_{\text{lab}} \simeq 1.5$ –2; for larger values of y_{lab} the invariant cross sections increase very slowly and seem to reach a plateau. The length of such a plateau depends on the transverse momentum p_t , decreasing when p_t increases (see fig. 5.6). But even at ISR energies the plateau, suggested for instance by the short-range order hypothesis, has not been completely reached. It should be noticed that, while it is not possible to distinguish the central from the fragmentation region when the data are plotted as a function of x , these features are clearly separated when they are plotted as a function of y_{lab} .

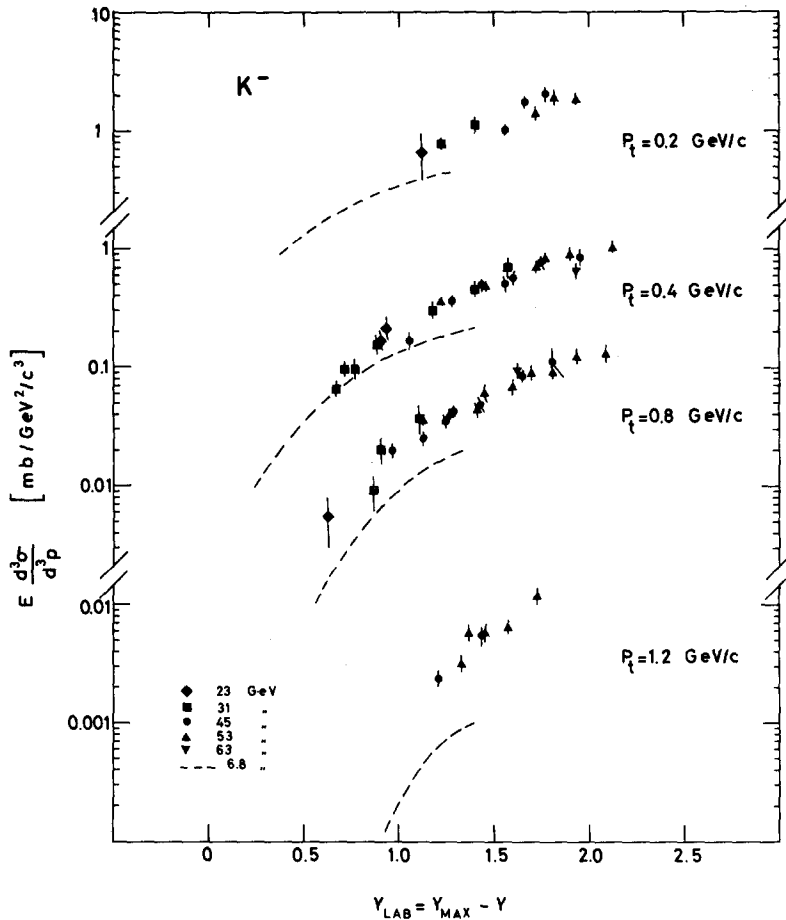


Fig. 5.9. The invariant cross sections for K^- production versus y_{lab} at fixed values of p_t .

This separation is still clear for proton production, where leading particle effects substantially modify the shape of the y_{lab} distribution. It is felt, therefore, that y_{lab} is a more meaningful variable with which to present these data.

6.2. Dependence on transverse momentum

The transverse momentum distributions have been discussed in detail in a previous paper [8]. Therefore only the more relevant features will be reported here. From the analysis of the transverse momentum distributions at fixed x or y_{lab} , it appears that a simpler description of particle production is obtained in terms of p_t and y_{lab} . At

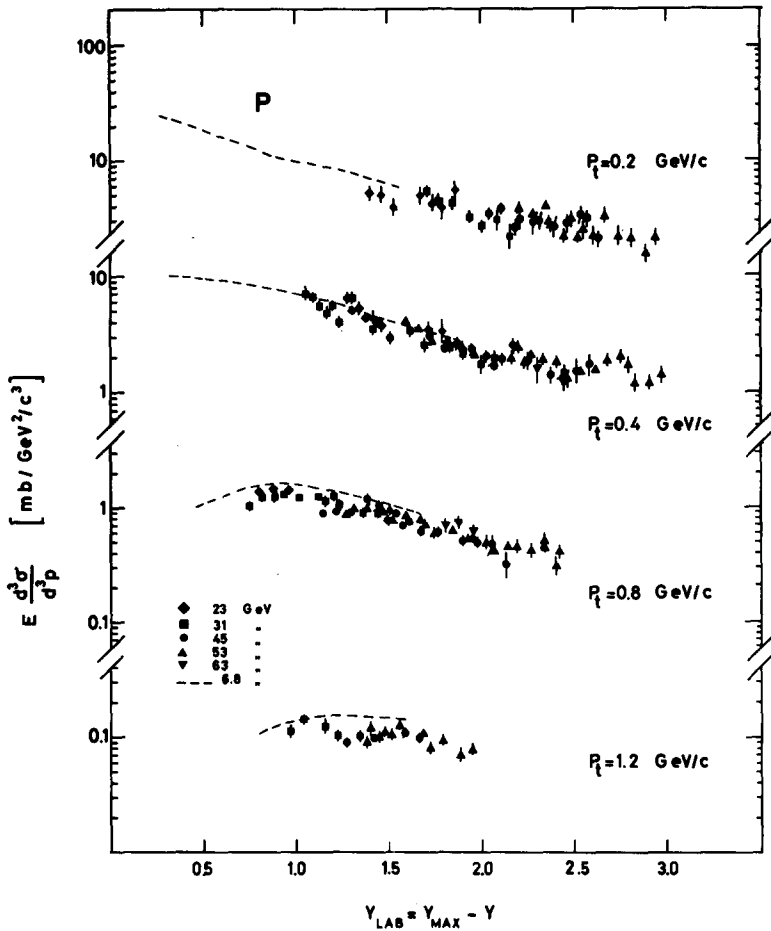


Fig. 5.10. The invariant cross sections for proton production *versus* y_{lab} at fixed values of p_t .

fixed y_{lab} , the invariant cross sections for pions and kaons are purely exponential in p_t , at least in the range of transverse momenta measured in this experiment ($0.15 < p_t < 1.2 \text{ GeV}/c$). The distributions seem to be Gaussian for antiprotons, while for protons they are Gaussian in the fragmentation region and exponential in the central region (fig. 5.18) [8].

For all particles the average values of the transverse momenta at fixed values of the laboratory rapidity $\langle p_t \rangle_y$ increase with y_{lab} until y_{lab} reaches 2. For pions with y_{lab} greater than 2, $\langle p_t \rangle_y$ appears to increase slightly, i.e. by less than 10%, as a function of y_{lab} . However, within the experimental errors the data are also consistent with $\langle p_t \rangle_y$ being constant in this region ($\langle p_t \rangle_y \simeq 320 \text{ MeV}/c$). Therefore in the cen-

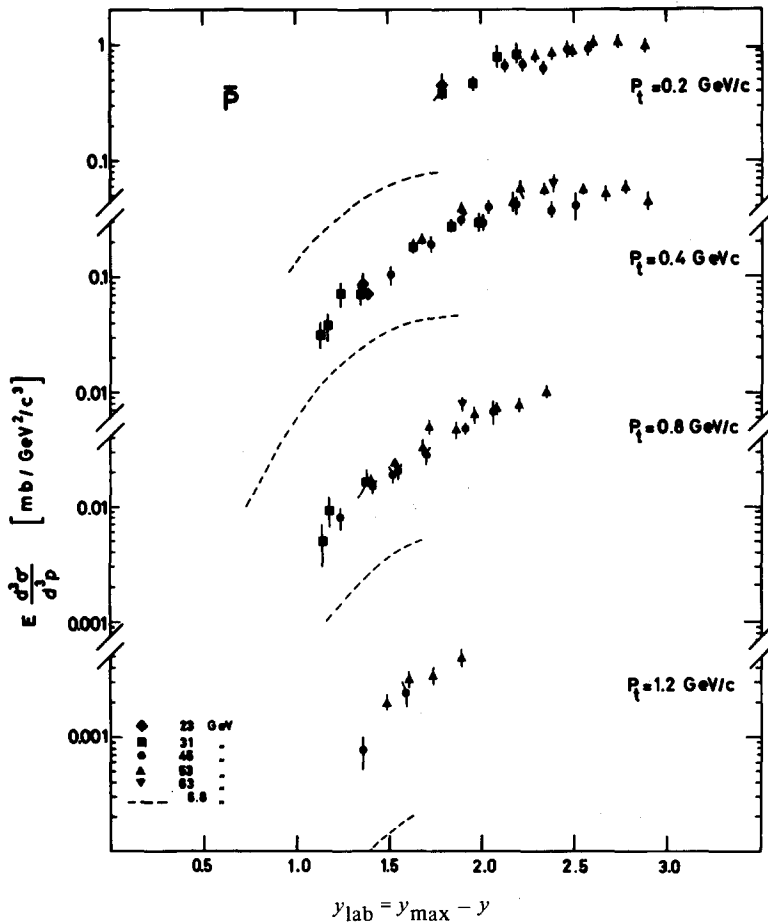


Fig. 5.11. The invariant cross sections for antiproton production *versus* y_{lab} at fixed values of p_t .

tral region the factorization of the cross section in y_{lab} and p_t seems to be a good approximation within 5–10%. In the range of y_{lab} explored by the present experiment, $\langle p_t \rangle_y$ is about 450 and 400 MeV/c for K^+ and K^- and 500 MeV/c for protons and antiprotons. The average transverse momentum of each particle is a little larger than the value of the corresponding antiparticle.

6.3. Energy dependence

The invariant cross sections will now be briefly discussed in terms of their energy dependence. The first thing to be looked at is the energy dependence within the ISR

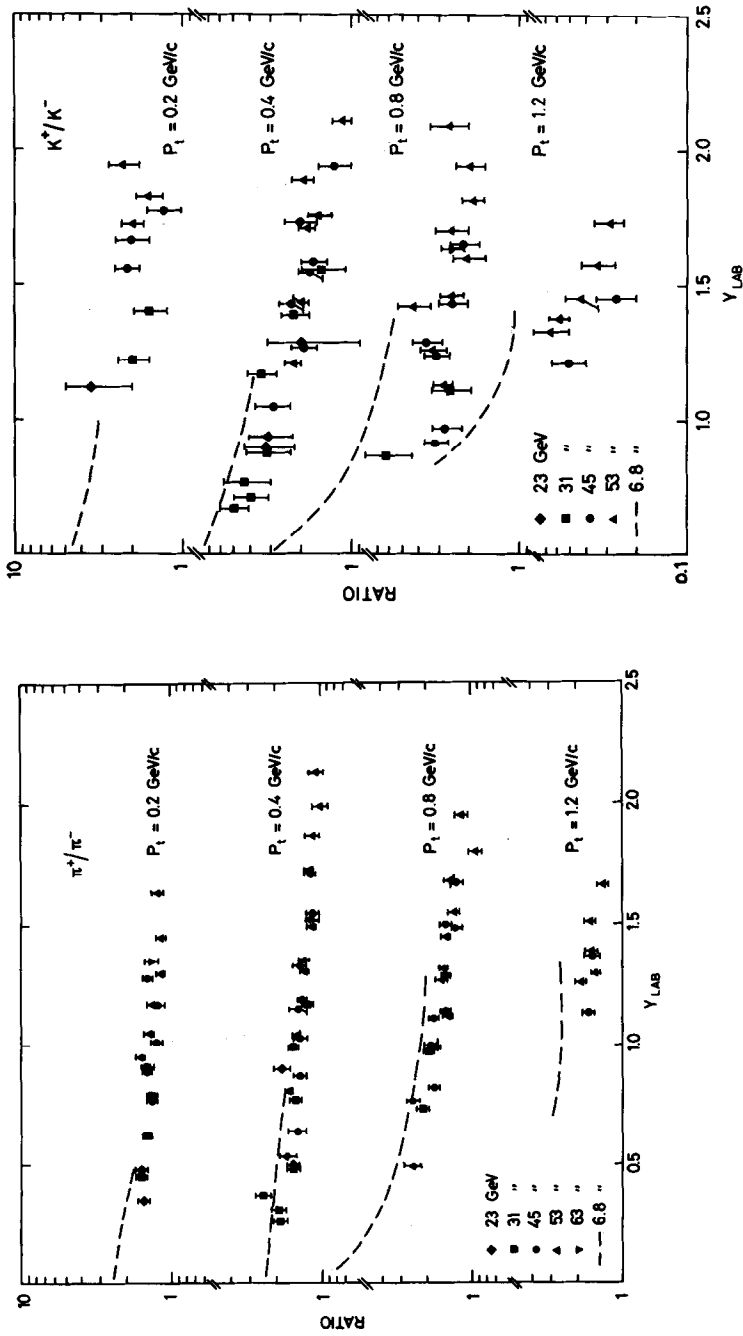


Fig. 5.12. Particle-to-antiparticle ratios as a function of Y_{LAB} at fixed values of p_t : π^+/π^- , K^+/K^- .

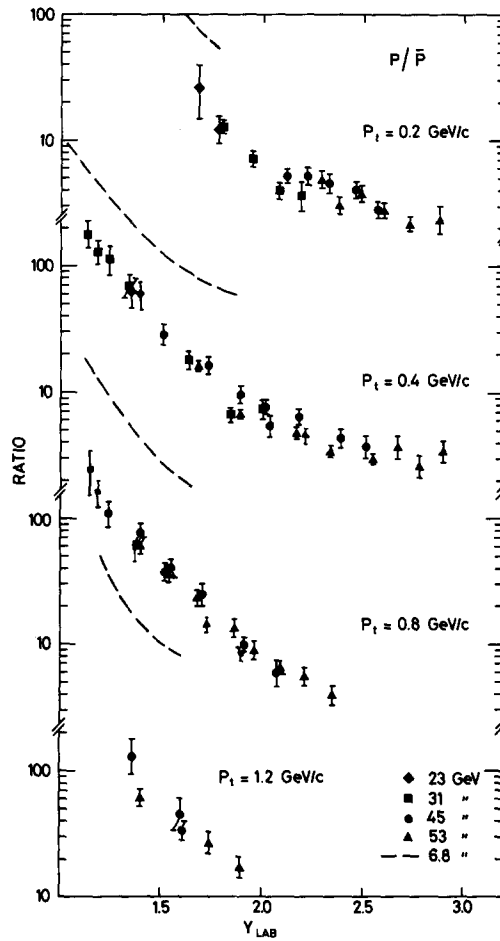


Fig. 5.13. Proton-to-antiproton ratios as a function of y_{lab} at fixed values of p_t .

energy range, i.e. from 23 to 63 GeV c.m. energy. The comparison of the cross sections measured at different ISR energies (figs. 5.1. to 5.11), at the same values of y_{lab} (or x) and p_t , shows that within errors there is no energy dependence for the production of π^\pm , K^\pm , and p in the explored range of y_{lab} and p_t ; the data points for each particle follow the same “curve” on y_{lab} and p_t , independently of the ISR energy. For K^- and \bar{p} no energy dependence has been observed above 45 GeV c.m. energy, while some energy dependence appears below, as can be seen in fig. 5.17 and ref. [8]. It should be noted that the overlapping between the data taken at different ISR energies was limited by the acceptance of our spectrometer, and that few measurements

were performed at 23 and 63 GeV c.m. energy.

As far as the onset of scaling is concerned, our data should be compared with lower energy results. This has been done in figs. 5.1 to 5.11, where dashed lines represent the low-energy data ($E_{\text{c.m.}} = 6.8$ GeV) of Allaby et al., [19] obtained in a counter experiment and those of Blobel et al. [20] from a bubble chamber experiment: for pions, the average value of the two experiments has been plotted, while for kaons, protons, and antiprotons only the data of Allaby et al. were used. Both experiments quoted overall errors of about 5–15%. As already stated, in the comparison between data at low and high energies, the y_{lab} variable was preferred instead of the x variable, since the former differentiates neatly between fragmentation and central regions: in fact secondaries emitted with small values of x are at low energy still in the fragmentation region, while at ISR energies they are in the central region.

The invariant cross sections for pion production increase slightly from PS to ISR energies in the central region. For π^- , fig. 5.7 shows no energy dependence in the fragmentation region, while for π^+ the situation may be more complex: in fact the π^+ cross sections at small y_{lab} seem to decrease somewhat between PS and ISR energies (fig. 5.6). The differences in the energy dependence for π^+ and π^- is clearly seen in fig. 5.12: the ratio π^+/π^- decreases from PS to ISR energies, indicating that the scaling region is reached first by π^+ 's and later by π^- 's.

For K^+ the cross sections increase from PS to ISR energies in the central region and are energy-independent in the fragmentation region (fig. 5.8). For K^- the ISR results are always larger than the lower-energy data, the difference increasing with p_t . The ratio K^+/K^- , shown in fig. 5.12, is lower at ISR energies. From fig. 5.14, where the ratios K^+/π^+ and K^-/π^- grow with energy, it is clear that scaling is reached sooner for pions than for kaons.

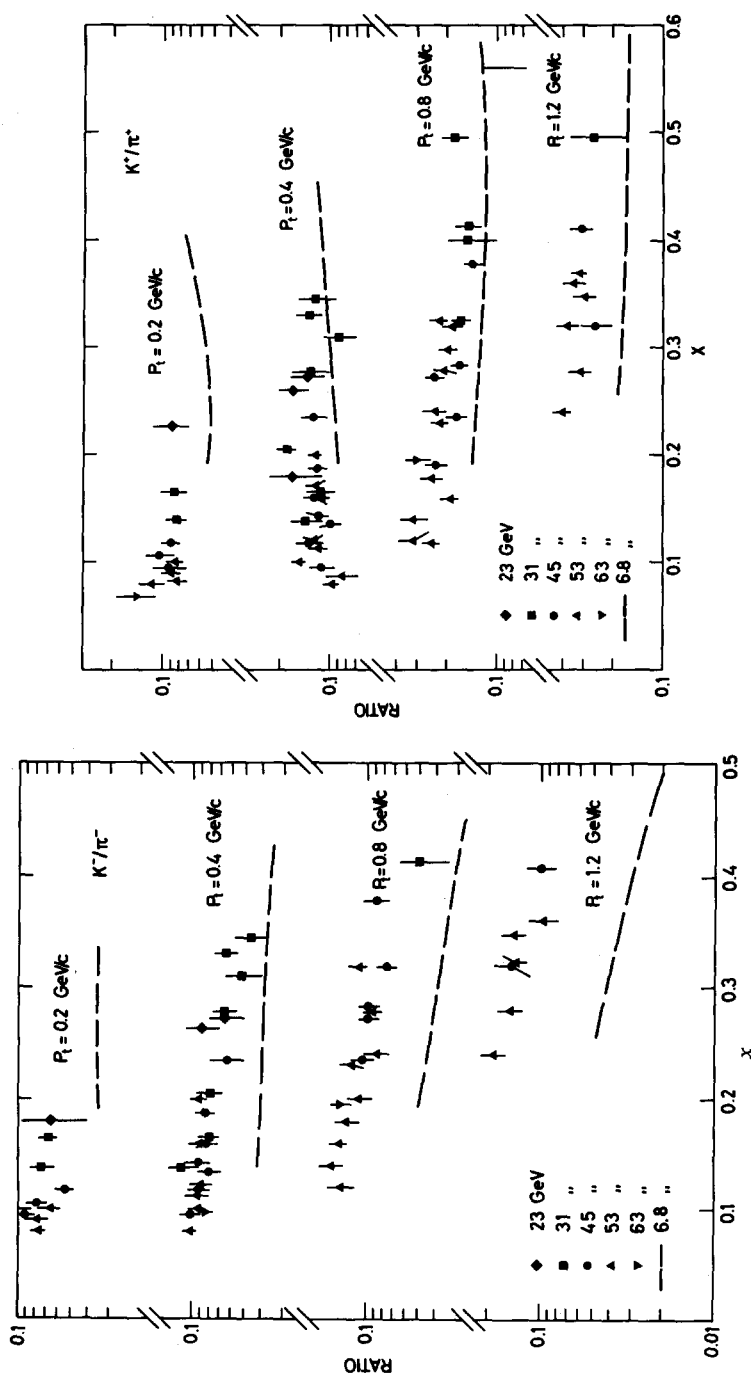
The ISR proton cross sections are a little smaller than at PS energy, the difference increasing with p_t (fig. 5.10). For the antiprotons, fig. 5.11 shows a large rise of the cross section with increasing energy. This is also evident in fig. 5.13, where the ratio p/\bar{p} is much smaller at ISR energies. From fig. 5.16, it is clear that scaling is reached much later for antiprotons than for pions. The ratio p/π^+ shown in fig. 5.15, decreases from PS to ISR energies, the difference being smaller with increasing values of x .

A more detailed discussion of the energy dependence will be the subject of a forthcoming paper.

6.4. Particle composition

The particle ratios are very useful for comparing the behaviour of the production processes for the various secondaries.

At fixed values of p_t , the particle-to-antiparticle ratios, shown in fig. 5.12, decrease with increasing y_{lab} ; the effect becomes more pronounced for larger p_t values and for heavier particles. All particle-to-pion ratios (figs. 5.14 to 5.16) decrease with increasing x , except p/π^+ which increases, reflecting the effect of the leading proton. A compilation of the particle ratios obtained at the ISR is presented in fig. 6.2, for

Fig. 5.14. K^*/π^+ and K^-/π^- ratios as a function of x at fixed values of p_T .

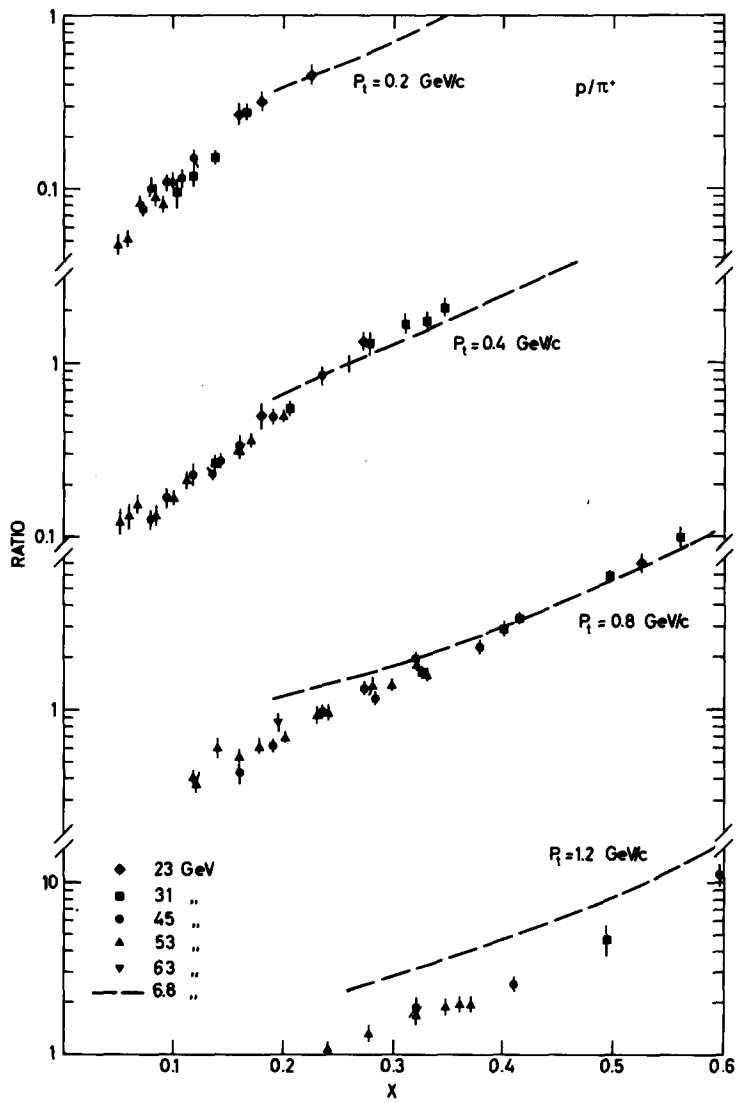


Fig. 5.15. p/π^+ ratios as a function of x at fixed values of p_t .

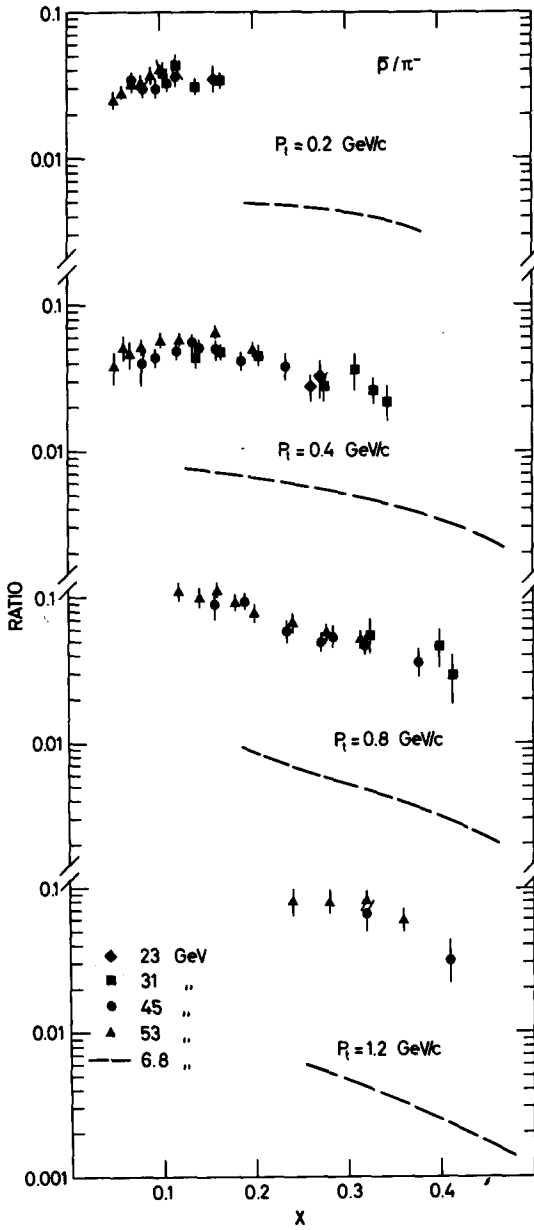


Fig. 5.16. \bar{p}/π^- ratios as a function of x at fixed values of p_t .

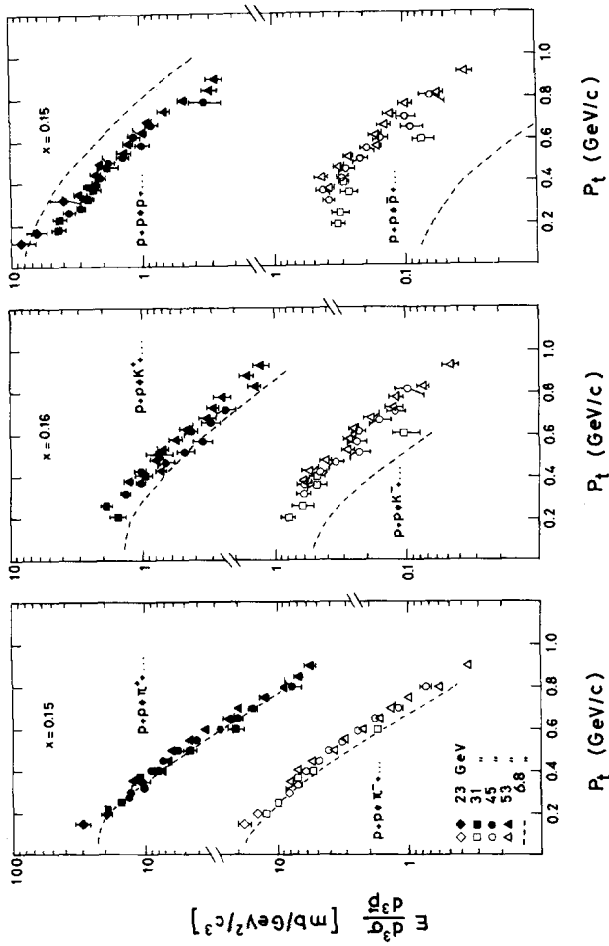


Fig. 5.17. The invariant cross-sections versus transverse momentum at a value $x \approx 0.16$ for the production of pions, kaons, protons, and anti-protons.

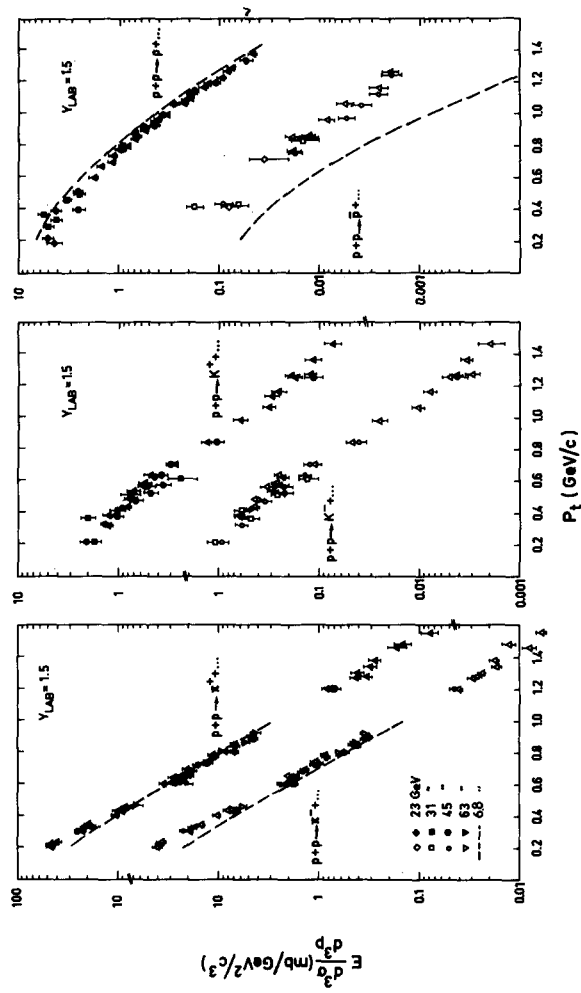


Fig. 5.18. The invariant cross sections versus transverse momentum at a value $y_{lab} = 1.5$ for the production of pions, kaons, protons, and anti-protons.

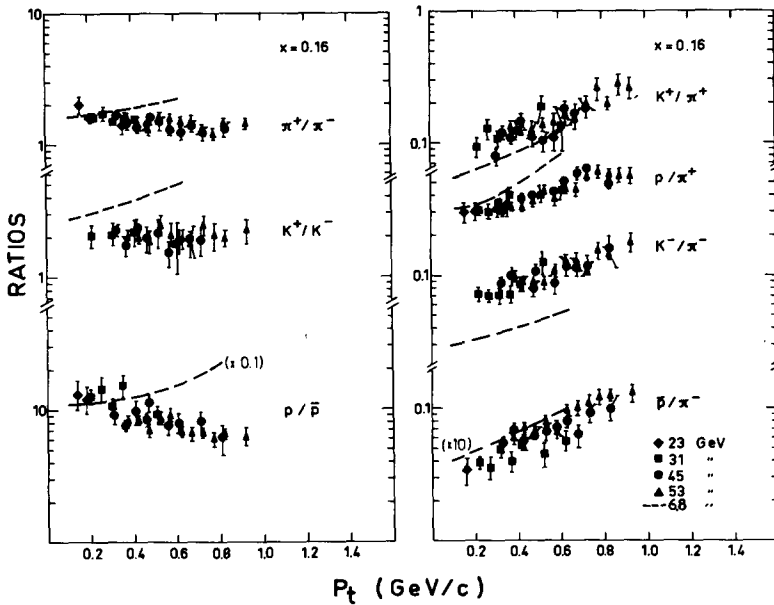


Fig. 5.19. Particle ratios *versus* transverse momentum at a value $x = 0.16$.

$p_t = 0.4$ GeV/c: the ratios π^+/π^- and K^+/K^- approach 1 in the central region, as expected at asymptotic energies, while the p/\bar{p} ratio is still of the order of 2. This confirms that the asymptotic energy region is not reached for \bar{p} . The particle-to-pion ratios are about 0.1 in the central region, indicating that, even at such very high energies, the overwhelming part of the produced secondaries are still the pions.

These ratios are also presented in figs. 5.19 and 5.20, as a function of the transverse momentum p_t , for fixed values of $x = 0.16$ and $y_{lab} = 1.5$, respectively. All the particle-to-pion ratios increase with p_t , in agreement with recent results at high transverse momentum [24]. For $y_{lab} = 1.5$, these ratios show a flattening off, starting at $p_t = 1.2$ GeV/c. The particle-to-antiparticle ratios vary only slightly with p_t .

The charged particle composition has been computed as a function of y_{lab} and p_t . The results obtained at $p_t = 0.4$ GeV/c as function of y_{lab} and at $y_{lab} = 1.5$ as function of p_t , are presented in table 6.1 and fig. 6.3. The errors were estimated to be 5% for pions and protons, and 10% for kaons and antiprotons. The relative proportion of each particle (except the leading proton) grows as a function of y_{lab} up to an almost constant value (maybe slightly increasing) in the central region. As a function of p_t , the relative proportion of the massive particles increases, while that of the pions decreases. The ratio of the positive to negative particles is also given in table 6.1. At $p_t = 0.4$ GeV/c, the ratio $+/-$ decreases rapidly towards 1 from the fragmentation to the central region. At $y_{lab} = 1.5$, the ratio $+/-$ increases with p_t , indicating an excess of positive particles at high transverse momentum [25].

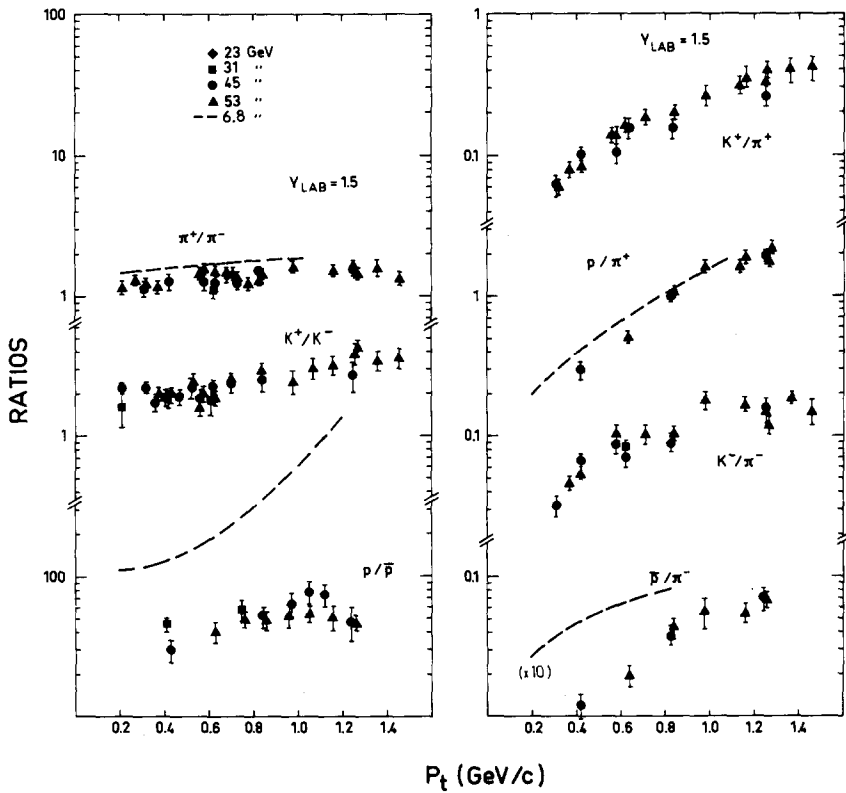


Fig. 5.20. Particle ratios versus transverse momentum at a value $y_{lab} = 1.5$.

6.5. Comparison with theoretical models

Many models have been proposed to describe particle production in inclusive reactions at very high energies [1, 26–28, 12, 14]. The Mueller-Regge formalism is at present widely used [1]. The predictions of the multiperipheral models have been capable of giving a reasonable description of high-energy particle production, in particular in the central region [26]. Diffraction-fragmentation models (“fireball”, “jet”, “nova”, etc.) have met with more success at large values of x [1, 27]. Some difficulties of these models have been overcome by “mixed” or “two-components” models [28]. The extensive computations of the statistical thermodynamic model of Hagedorn et al. [12] are in general agreement with our results. In the same class of models, the Landau hydrodynamical model gives a fairly simple description of inclusive distributions [14]. In the range of independent variables covered in this experiment, the prediction of the above-mentioned models are qualitatively consistent with our data.

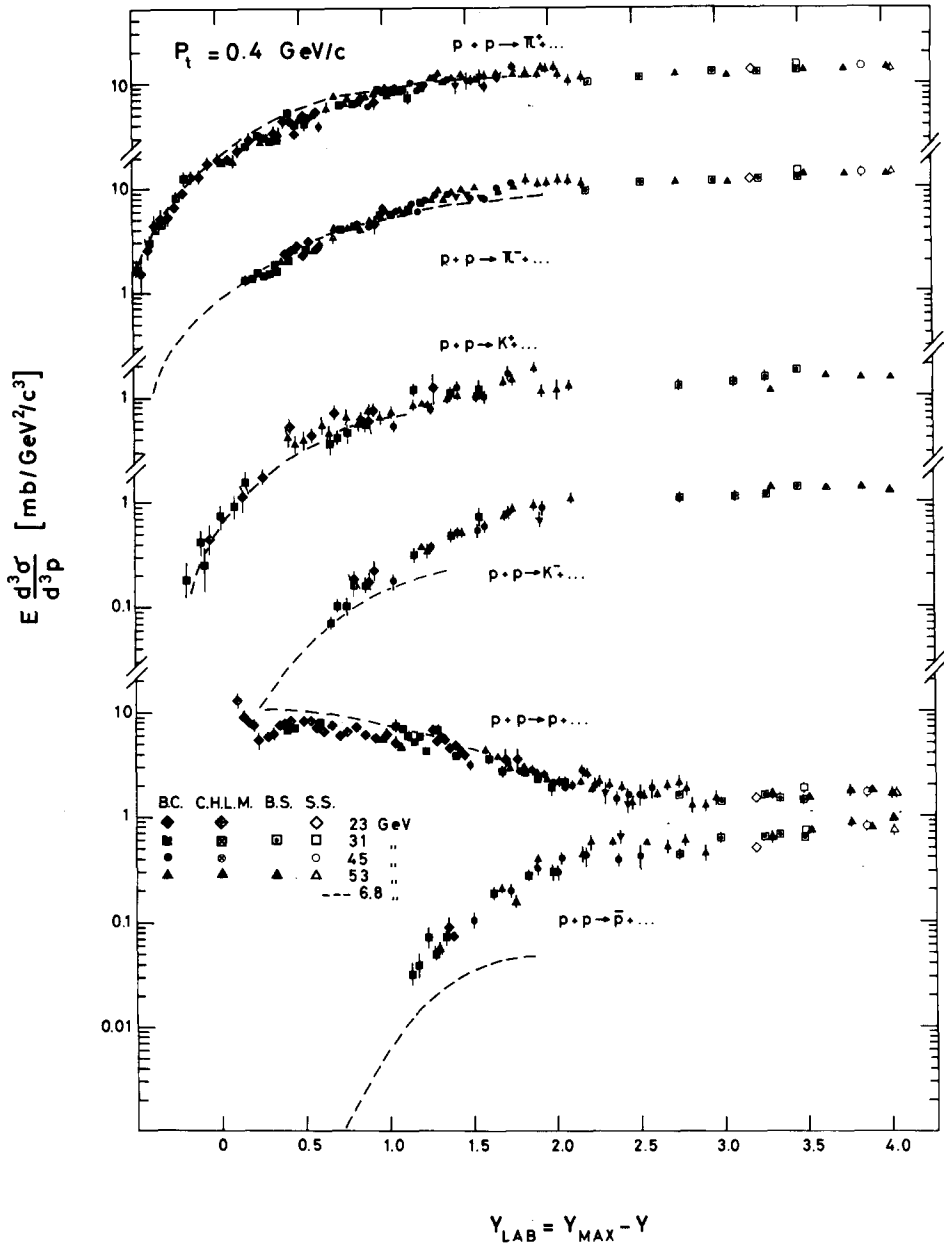


Fig. 6.1. The invariant cross sections for pions, kaons, protons, and antiprotons production *versus* y_{lab} at $p_t = 0.4$ GeV/c. The data points refer to: BC present experiment; CHLM ref. [23]; BS ref. [21]; SS ref. [22]; the dashed lines refer to low-energy data of refs. [19, 20].

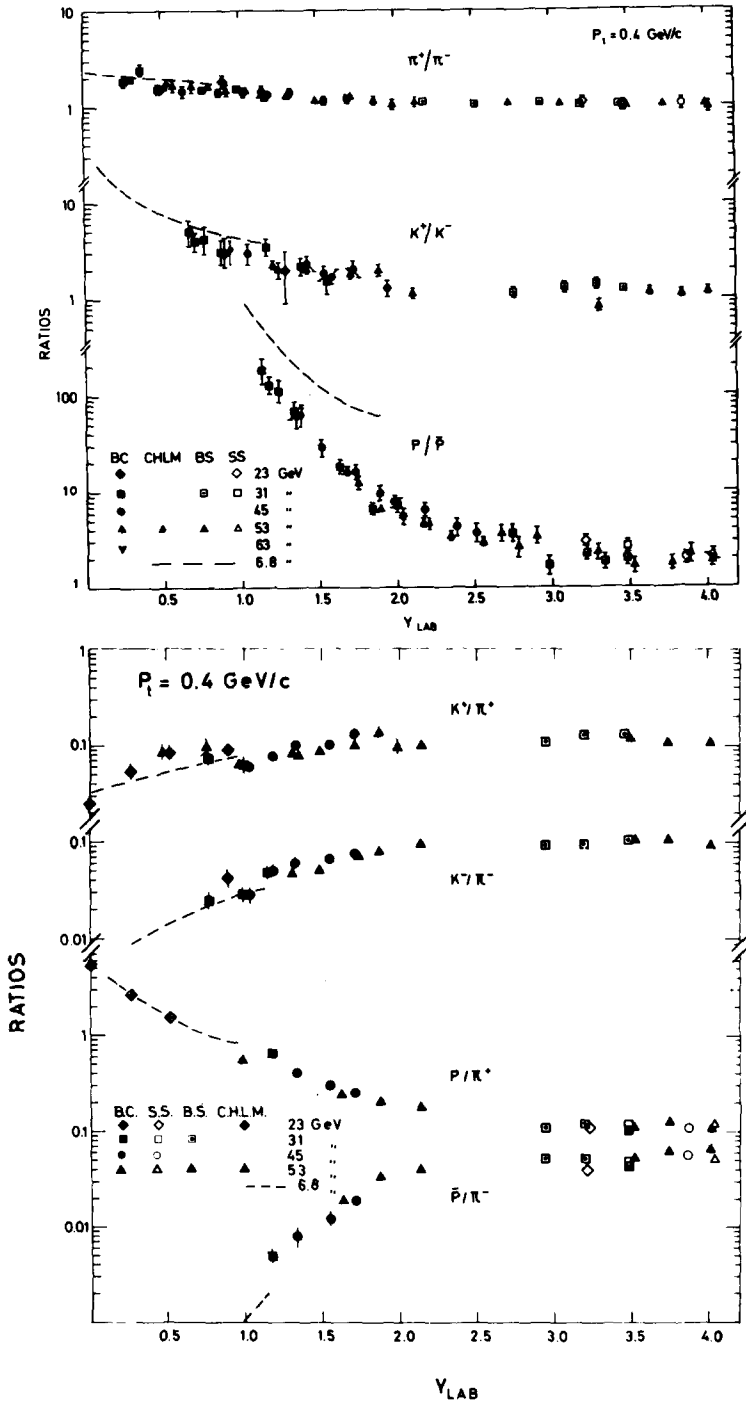


Fig. 6.2. Particle ratios versus y_{lab} at a value of $p_t = 0.4 \text{ GeV}/c$.

Table 6.1
Particle composition at $p_t = 0.4$ GeV/c and at $y_{lab} = 1.5$

p_t (GeV/c)	y_{lab}	π^+/ch	π^-/ch	K^+/ch	K^-/ch	p/ch	\bar{p}/ch	+/-
0.4	0.0	0.087	0.039	0.0029		0.87		20.0
	0.5	0.24	0.14	0.017	0.0015	0.60		6.1
	1.0	0.37	0.25	0.031	0.0087	0.34	0.0008	2.8
	1.5	0.44	0.36	0.040	0.021	0.15	0.0042	1.7
	2.0	0.43	0.40	0.043	0.035	0.076	0.012	1.2
	2.5	0.42	0.42	0.042	0.039	0.056	0.018	1.1
	3.0	0.44	0.41	0.044	0.037	0.051	0.020	1.1
	3.5	0.45	0.41	0.048	0.038	0.048	0.022	1.1
	4.0	0.43	0.40	0.047	0.040	0.050	0.025	1.1
0.2	1.5	0.48	0.43	0.021	0.012	0.059	0.0029	1.3
0.4		0.44	0.36	0.040	0.021	0.15	0.0042	1.7
0.6		0.37	0.31	0.054	0.027	0.23	0.0058	1.9
0.8		0.34	0.25	0.060	0.023	0.33	0.0072	2.6
1.0		0.29	0.21	0.066	0.023	0.40	0.0066	3.1
1.2		0.29	0.17	0.081	0.024	0.43	0.0078	4.0
1.4		0.25	0.16	0.10	0.028	0.46	0.0073	4.0

The values listed are the ratios of the invariant cross section for each particle to the sum of the invariant cross sections for all charged particles.

7. Conclusions

An extensive set of inclusive measurements of π^\pm , K^\pm , p , and \bar{p} production carried out at the CERN ISR has been presented. The results reported here and in ref. [8] allow a complete experimental picture of the production processes in a zone which covers part of both the fragmentation and central regions ($0 < y_{lab} < 3$), at medium transverse momenta ($0.15 < p_t < 1.5$ GeV/c).

The main conclusions reached may be summarized as follows:

(i) For all particles except protons the dependence of the invariant cross section on the x variable is faster than an exponential. In the experimental distributions plotted *versus* y_{lab} the distinction between central and fragmentation regions appears clearly. The "central plateau" for $y_{lab} > 2$ is actually increasing slowly with y_{lab} [21, 22]. The proton distributions have a different behaviour, showing features typical of a leading particle.

(ii) At fixed y_{lab} the dependence on transverse momentum is, to a good approximation, exponential for π^\pm and K^\pm production. The dependence for antiprotons and

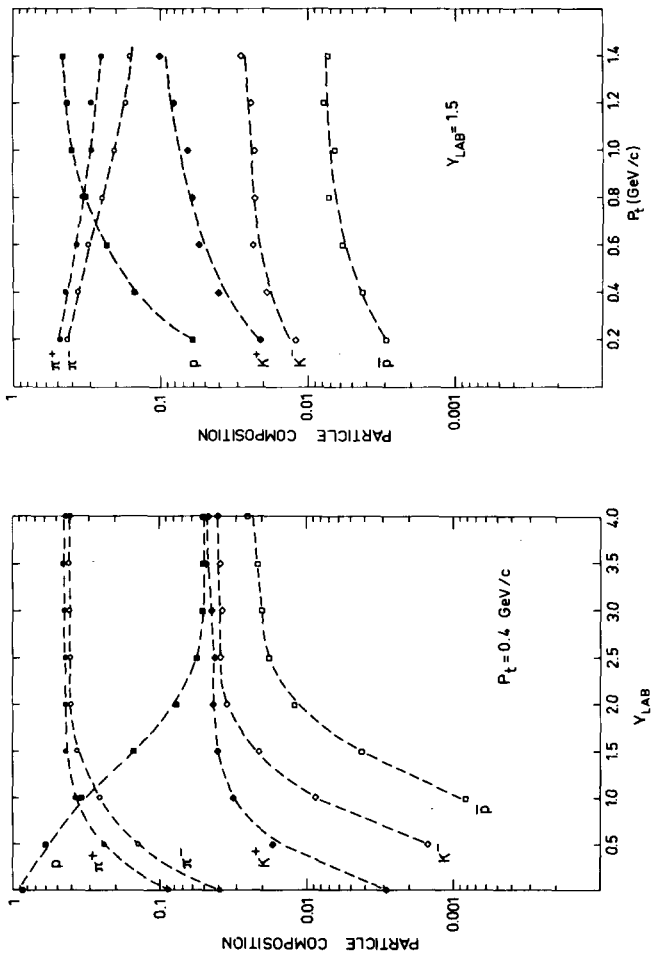


Fig. 6.3. Charged particle composition at $p_t = 0.4 \text{ GeV/c}$ and $Y_{LAB} = 1.5$. The points correspond to the ratios of the production cross section for each particle to the sum of the cross sections for all charged particles. The dashed lines are to guide the eye.

protons in the fragmentation region seems to be better represented with a Gaussian form [8].

(iii) The factorization of the invariant cross section in terms of y_{lab} and p_t is a reasonable approximation in the central region, at least for pions.

(iv) The ISR data exhibit no energy dependence, with the exception of the \bar{p} and maybe of the K^- below 45 GeV c.m. energy. The comparison with lower-energy data indicates that the approach to scaling is dependent on the type of produced particle, with a kind of hierarchy related at least to the mass and charge of the particle involved. Scaling is reached sooner in the fragmentation region than in the central region and sooner at low p_t than for larger p_t .

(v) Even at ISR energies, pion production is the dominant process; kaon production is of the order of 10% of the pion.

(vi) At the highest ISR energies the π^+/π^- and K^+/K^- ratios tend to 1 for $x \rightarrow 0$, the p/\bar{p} ratio tends towards 2.

We are grateful to K. Johnsen and to the ISR staff for their efficient operation of the machine, and to F. Bonaudi, G. Kantardjan and their crews for providing excellent supporting facilities. We acknowledge the contributions of many colleagues to different phases of the experiment: A. Albini, M. Antinucci, B.A. Babcock, A. Cristallini, M.D'Agostino-Bruno, D.D'Alessandro, A.D. Krisch, C. Maroni, F. Mercatali, R.T. Poe, L.G. Ratner and J.B. Roberts. The competent technical assistance of G. Busacchi, O. Ferrari and M. Mignardi is acknowledged.

References

- [1] M. Jacob, Rapporteur's talk at the 16th Int. Conf. on high energy physics, Batavia, Ill., 1972 (NAL, Chicago-Batavia, 1972), vol. 3, p. 373; Lectures at the 1973 CERN-JINR School of Physics, CERN-73-12, 1973.
- [2] R.P. Feynman, Phys. Rev. Letters 23 (1969) 1415.
- [3] J. Beneke, T.T. Chou, C.N. Yang and E. Yen, Phys. Rev. 188 (1969) 2159.
- [4] A. Bertin, P. Capiluppi, A. Cristallini, M.D'Agostino-Bruno, R.J. Ellis, G. Giacomelli, C. Maroni, F. Mercatali, A.M. Rossi and G. Vannini, Phys. Letters 38B (1972) 260.
- [5] A. Bertin, P. Capiluppi, M.D'Agostino-Bruno, R.J. Ellis, G. Giacomelli, A.M. Rossi, G. Vannini, A. Bussi re and R.T. Poe, Phys. Letters 41B (1972) 201.
- [6] A. Bertin, P. Capiluppi, M. D'Agostino-Bruno, R.J. Ellis, G. Giacomelli, A.M. Rossi, G. Vannini, A. Bussi re and R.T. Poe, Phys. Letters 42B (1972) 493.
- [7] M. Antinucci, A. Bertin, P. Capiluppi, M. D'Agostino-Bruno, G. Giacomelli, A.M. Rossi, G. Vannini, and A. Bussi re, Nuovo Cimento Letters 6 (1973) 121.
- [8] P. Capiluppi, G. Giacomelli, A.M. Rossi, G. Vannini and A. Bussi re, Nucl. Phys. B70 (1974) 1.
- [9] K. Johnsen, Nucl. Instr. 108 (1973) 205; E. Keil, CERN 72-14 (1972).
- [10] S. Van der Meer, Calibration of the effective beam height in the ISR, Internal report CERN-ISR-PO/68-31 (1968).

- [11] L.G. Ratner, R.J. Ellis, G. Vannini, B.A. Babcock, A.D. Kirsch and J.B. Roberts, *Phys. Rev. Letters* 27 (1971) 68; *Phys. Rev. D* 9 (1974) 1135.
- [12] R. Hagedorn, CERN 71-12 (1971).
- [13] CERN PS Users Handbook.
- [14] P. Carruthers and Minh Duong Van, *Phys. Rev. D* 8 (1973) 859.
- [15] K. Potter and J.C. Sens (eds.), CERN NP Internal report 71-6 (1971).
- [16] D. Barber and B. Bosnjakovic, CERN NP Internal note (1973), unpublished.
- [17] D. Barber, K. Potter and F. Van der Meer, Luminosity measurements by the Van der Meer method at the ISR, CERN-ISR internal report (1973), unpublished.
- [18] R.J. Abrams, R.L. Cool, G. Giacomelli, T.F. Kycia, B.A. Leontic, K.K. Li, A. Lundby, D.N. Michael and J. Teiger, *Phys. Rev. D* 4 (1971) 3235;
S.P. Denisov, S.V. Donskov, Yu.P. Gorin, R.N. Krasnokutsky, A.I. Petrukhin, Yu.D. Prokoshkin and D.A. Stoyanova, *Nucl. Phys. B* 61 (1973) 62.
- [19] J.V. Allaby, A.N. Diddens, R.W. Dobinson, A. Klovning, J. Litt, L.S. Rochester, K. Schlüpmann, A.M. Wetherell, U. Amaldi, T. Biancastelli, C. Bosio and G. Mathiae, Contribution to the 4th Int. Conf. on high-energy collisions, Oxford, 1972 (Rutherford High-Energy Laboratory, Didcot, England, 1972), vol. 2, p. 85.
- [20] V. Blobel, G.W. Brandenburg, H. Fesefeldt, H. Franz, B. Hellwig, V. Idschok, D. Mönkemeyer, H.J. Mück, N.F. Neuman, H. Schachter, N. Schmitz, W. Schranel, D. Schwarz, G.M. Schwarzschild, F. Selonke, P. Söding and B. Wessels, DESY report 73/36 (1973).
- [21] B. Alper, P. Booth, A. Bøggild, F. Bulos, L.J. Carroll, G. Damgaard, G. von Dardel, B. Duff, F.F. Heymann, J.N. Jackson, G. Jarlskog, L. Jonsson, A. Klovning, L. Leistam, E. Lillethun, G. Lynch, M. Prentice, D. Quarrie and J. Weiss, *Phys. Letters* 47B (1973) 75, 275.
- [22] M. Banner, J.L. Hamel, J.P. Pansart, A.V. Stirling, J. Teiger, H. Zacccone, J. Zsemsbery, G. Bassompierre, M. Croissiaux, J. Gresser, R. Morand, M. Riedinger and M. Schneegans, Paper presented at the 16th Int. Conf. on high-energy physics, Batavia, Ill., 1972; *Phys. Letters* 41B (1972) 547.
- [23] M.G. Albrow, D.P. Barber, A. Bogaerts, B. Bosnjaković, J.R. Brooks, A.B. Clegg, F.C. Ern , C.N.P. Gee, A.D. Kanaris, D.H. Locke, F.K. Loebinger, P.G. Murphy, A. Rudge, J.C. Sens, K. Terwilliger and F. Van der Veen, *Phys. Letters* 42B (1972) 279; *Nucl. Phys. B* 56 (1973) 333, and *Phys. Letters*, to be published.
- [24] B. Alper, A. Bøggild, G. Jarlskog, G. Lynch, J.M. Weiss, P. Booth, L.J. Carroll, J.M. Jackson, M. Prentice, G. von Dardel, L. Jonsson, G. Damgaard, K.H. Hansen, E. Lohse, F. Bulos, L. Leistam, A. Klovning, E. Lillethun, B. Duff, F. Heymann, D. Quarrie and S.S. Harrock, *Phys. Letters* 44B (1973) 521, 527.
- [25] M. Banner, J.L. Hamel, J.P. Pansart, A.V. Stirling, J. Teiger, H. Zacccone, J. Zsemsbery, G. Bassompierre, M. Croissiaux, J. Gresser, R. Morand, M. Riedinger and M. Schneegans, *Phys. Letters* 44B (1973) 537.
- [26] G. Costa and P. Pasti, *Rev. Fis. (Brazil)* 3 (1973) 87.
- [27] R. Slansky, High-energy hadron production and inclusive reactions, Yale R-3075-50 (1973).
- [28] C. Quigg, Lectures at the Canadian Institute of Particle Physics, 1973, McGill University.